Optical Resonances of Glass Microspheres in Amorphous and Crystalline Liquids

by

Hasan Yılmaz

A Thesis Submitted to the
Graduate School of Sciences and Engineering
in Partial Fulfillment of the Requirements for
the Degree of

Master of Science

in

Materials Science and Engineering

Koç University

January 2011

Koç University

Graduate School of Sciences and Engineering

This is to certify that I have examined this copy of a master's thesis by

Hasan Yılmaz

and have found that it is complete and satisfactory in all respects,
and that any and all revisions required by the final
examining committee have been made.

Committee Members:

_____

Ali Serpengüzel, Ph. D. (Advisor)

_____

Erdem Alaca, Ph. D.

_____

Kaan Güven, Ph. D.

Date: _____

ABSTRACT

Optical microcavities have found many applications in linear optics, nonlinear optics, quantum optics, and biophotonics as laser light sources as well as optical switching, sensing, and wavelength division multiplexing devices. Microspheres are high quality factor optical microcavities that localize light by total internal reflection. Electromagnetic boundary conditions have to be satisfied for the light localization. Optical resonances occur, when an integer multiple of the wavelength is equal to the optical pathway of the cavity.

In this work, the polarization dependence of the optical resonances in an optical fiber-microsphere system is investigated experimentally. The change of the elastic light scattering spectra of the microspheres is studied for microspheres placed in various fluids. It is observed that, the shape of resonances and the intensity of the background are strongly dependent on the surrounding fluid medium. Blue and red shifts of the optical resonances are observed due to the changes of the external fluid media. This optical geometry heralds new device designs and applications for microsphere based optoelectronics and microfluidics.

ÖZET

Optik mikroçınlaçların doğrusal optik, doğrusal olmayan optik, kuvantum optik ve biyofotonik gibi alanlarda lazer kaynağı, optik anahtarlama, algılama ve dalgaboyu alanında çoğullama gibi yeni uygulamaları vardır. Mikroyuvarlar ışığı toplam tam yansıma ile yerelleyen yüksek kalite faktörlü mikroçınlaçlardır. Işığın yerelleşmesi için elektromanyetik sınır koşullarının sağlanması gerekir. Optik çınlama, yerelleşecek ışığın dalgaboyu optik yolun tam katlarına eşit olduğunda sağlanır.

Bu çalışmada optik mikroyuvar – lif düzeneğinin optik çınlamalarının kutuplanma bağıntısı deneysel olarak incelendi. Değişik akışkan ortamlardaki mikroyuvarların elastik ışık saçılmasındaki değişimler üzerine çalışıldı. Çınlamaların biçimlerinin ve arkaplan im gücünün ortamdaki sıvıya karşı çok duyarlı bir biçimde değiştiği gözlemlendi. Bu optic yapı mikroyuvar tabanlı optoelektronik ve mikroakışkanlık alanında yeni aygıt tasarımları ve uygulamaları sunmaktadır.

ACKNOWLEDGEMENTS

I am grateful to my advisor Prof. Ali Serpengüzel for his support, supervision, and guidance during this study. He showed me how an experimental physicist should be.

I would like to thank Asst. Prof. Erdem Alaca and Asst. Prof. Kaan Güven for participating as committee members in my thesis and their valuable feedback.

I also owe thanks to Asst. Prof. Oğuzhan Gürlü for guiding me to Koç University as well as his help in alignment and calibration of the dye laser, and Mehmet Selman Tamer for the control and data acquisition software development.

I would like to indicate my deep gratitude to my Microphotonics Research Laboratory partners and friends; Emre Yüce, Mohammed Sharif Murib, Kurt David Webb, Ersin Hüseyinoğlu, Huzeyfe Yılmaz, Ulaş Sabahattin Gökay, and Seyed Alireza Aleali for their valuable scientific discussions and their friendship.

This thesis would have never existed without the support of my family. I would like to thank them for their love and support throughout my life.

Lastly, I would like to acknowledge Türkiye Bilimsel ve Teknolojik Araştırma Kurumu (TÜBİTAK) grant No. EEEAG - 106E215 and European Commission (EC) grant No's FP6-IST-003887 NEMO and FP6-IST-511616 PHOREMOST for their financial support to our research.

This thesis is dedicated to my parents and my brother; Ozan.

TABLE OF CONTENTS

LIST OF FIGURES

NOMENCLATURE

a	Microsphere radius
a_n	Transverse magnetic mode elastic scattering field coefficient
b	Impact parameter
b_n	Transverse electric mode elastic scattering field coefficient
c_n	Transverse magnetic mode internal field coefficient
d_n	Transverse electric mode internal field coefficient
E	Electric field amplitude
$h_n^1(x)$	Spherical Hankel function of the first kind
$h_n^2(x)$	Spherical Hankel function of the second kind
$j_n(x)$	Spherical Bessel function
k	Wave vector
K_{11}	Splay deformation constant of the liquid crystal
K_{22}	Twist deformation constant of the liquid crystal
K_{33}	Bend deformation constant of the liquid crystal
l	Radial mode order of the MDR
m	Angular mode number of the MDR
m	Relative refractive index
n	Polar angular mode number of the MDR
n_1	Refractive index of the medium
n_2	Refractive index of the microsphere
n_e	Extraordinary refractive index
n_o	Ordinary refractive index
$\hat{n}$	Director vector of the liquid crystal

ω	Optical angular frequency
Q	Quality factor of the MDR
Q_{abs}	Quality factor associated with the absorption losses
Q_{cont}	Quality factor associated with the surface contaminants
Q_e	Quality factor associated with the coupling losses
Q_{rad}	Quality factor associated with the radiation losses
Q_s	Quality factor associated with the scattering losses
t	Transmission coefficient through the optical fiber
x	Size parameter of the microsphere
U_{tw}	Threshold voltage of a twisted nematic cell
$\Delta\lambda$	Interpolarization mode spacing in wavelength
$\Delta\lambda_p$	Intrapolarization mode spacing in wavelength
$\delta\lambda$	Wavelength shift
ε	Permittivity of the medium
θ	Polar angle
λ	Wavelength of light in vacuum
κ	Coupling coefficient from the optical fiber to the microsphere
$\Delta\lambda_{1/2}$	Linewidth of an MDR
ν	Frequency of light
$\Delta\nu_{1/2}$	Linewidth of the MDR in frequency

Chapter 1

INTRODUCTION

Optical microcativies are devices with special geometries and materials that are optimized for optical resonances. Similar to whispering gallery modes of acoustic waves, light waves in an optical microcavity have resonance modes [1]. Various geometries are used for light localization, such as Fabry-Perot cavity [2], microdisk [3], microring [4], photonic crystal [5], microtoroid [6] and microsphere [7] geometries. The high symmetry of the microsphere brings many advantages to this geometry for easy fabrication, low cost, high quality resonances, possibility of three dimensional integration, and relatively easy numerical modeling [26]. High quality factor of the resonance of microspheres attracts the attention of many scientists from various disciplines for device applications with extremely high sensitivity. Numerous device applications are being studied in photonics, materials science, chemistry, electronics, and mechanical engineering. In the fields other than photonics, most device applications are based on shifting the optical resonances of microspheres. Spectral shift of resonances can be achieved by tuning the optical pathway of light in the microsphere. Mechanical stress [8,9], thermooptical [10], electrooptical [11, 12] effects, adsorbing molecules on the surface of the microsphere [13], chemical etching of the microsphere [14], and tuning the medium of the microsphere [15,16] are some examples using the resonances for stress, temperature, electrooptical, biological, and refractive index sensor applications.

Using the optical anisotropy of nematic liquid crystals is another recent innovation for tuning the resonances of the microsphere [17]. Recently, scientists also achieved the generation of nematic liquid crystal droplets in a polymer matrix [18, 19].

In chapter 2, a brief introduction to the geometrical and wave optics of spherical particles is given. Then, the necessary theoretical background including special Lorenz-Mie theory, and generalized Lorenz-Mie theory are explained. General properties of the morphology dependent resonances are defined. Finally, various coupling methods are introduced for coupling light to the microspheres.

In chapter 3, structural properties of the nematic liquid crystals and their applications are presented. The optical and electrooptical properties of the liquid crystal used in our experiments are explained. Finally, the most common method to control the birefringency of a nematic liquid crystal cell, the twisted nematic cell, is introduced.

Chapter 4 summarizes our experimental results on elastic light scattering from glass microspheres in various fluids. After the introduction of the experimental setup, the optics, the calibration process, and the material properties of the light sources, that are used in the experiments are explained. First experiments show the relation between the microsphere – optical fiber position, and the polarization dependence of the spectra. Later, the morphology dependent resonances of microspheres immersed in amorphous liquids and liquid crystals are analyzed. The change in the spectrum of microspheres with changing liquid medium is discussed. A solution for improving the signal of microsphere – optical fiber – liquid crystal system is suggested, and demonstrated with improved experimental results. Red and blue shift of resonances by placing and removing the liquid crystal is also presented in this chapter.

This thesis is concluded with chapter 5, which includes a summary of the work done and suggestions for future work. In the appendix, a brief manual is given for the control and data acquisition software using National Instruments LabView®.

Chapter 2

OPTICAL PROPERTIES OF DIELECTRIC SPHERES

2.1. Introduction

For optical devices much bigger than the wavelength and for low intensities, propagation of light can be explained by the laws of geometrical optics. If the light propagates in a homogenous medium, it follows straight lines of rays. When light meets an interface of two different homogenous media, some part of light reflects back, while some of it refracts. The light entering the second medium changes direction, obeying Snell's law, stated in the Eq. 2.1 [20],

$$n_1 \sin\theta_1 = n_2 \sin\theta_2 \tag{2.1}.$$

where n_1 is the refractive index of the surrounding medium, n_2 the refractive index of the inner medium, θ_1 the angle between the incoming ray and the normal to the surface, and θ_2 angle between the refracting ray and the normal to the surface. If the interface between the two media is curved, such as a sphere (shown in Fig. 2.1) the tangent plane is taken at the point, where the beam meets the interface. In the figure, the directly reflected ray (p_0), the directly transmitted ray (p_1) and the series of rays (p_2, p_3, …), that transmit after internal reflection are shown. However, geometrical optics cannot explain the ratio of the transmitted and reflected intensities. Fresnel formulae show that, the percentages depend on the angle of incidence and the polarization of light [21].

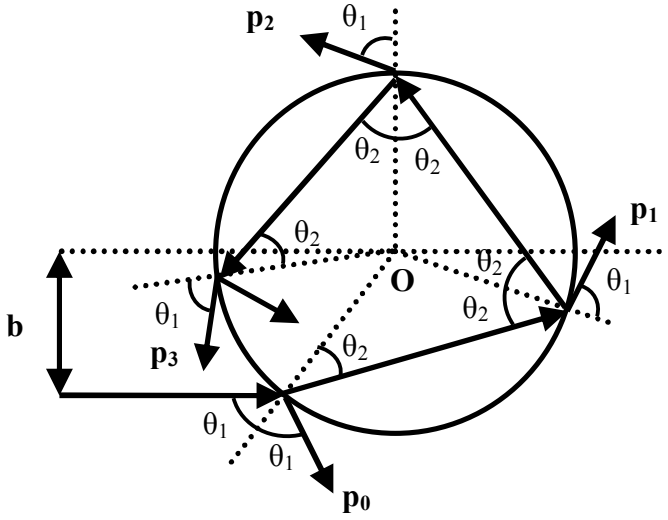

Figure 2.1 Scattering of a light ray from a spherical particle.

The distance between the center of the sphere and normal of the incoming ray's propagation direction is called the impact parameter (b). If the impact parameter is very close to the radius (a) of the sphere, a special type of internal reflection occurs. This is named as total internal reflection (TIR) in geometrical optics. Another theoretical approach is needed to explain the wave nature of light propagating inside the sphere. In the next section, a classical electrodynamics theory, called "special" Lorenz-Mie theory, will be threated for the scattering of plane wave from a dielectric sphere.

2.2. "Special" Lorenz-Mie Theory

When the wavelength of the light, interacting with a particle is larger than the size of the particle, the interaction between the light and the particle is explained by Rayleigh scattering. Interaction between spherical particles larger than the wavelength of the light is explained by the "special" Lorenz-Mie theory. "Special" Lorenz-Mie theory describes the scattering of plane wave from a dielectric spherical particle. By applying boundary conditions to Helmholtz equation for the electromagnetic waves, the scattered fields are expressed as spherical Bessel functions and spherical Henkel functions. For two different polarizations of light, called transverse magnetic (TM) and transverse electric (TE), the equations for scattered electric field amplitude coefficients can be expressed as a_n and b_n, respectively. The scattered field coefficients for the field outside the sphere are expressed as;

$$a_n = \frac{m^2 j_n(mx)\left[xj_n(x)\right]' - j_n(x)\left[mxj_n(mx)\right]'}{m^2 j_n(mx)\left[xh_n(x)\right]' - h_n(x)\left[mxj_n(mx)\right]'} \tag{2.2},$$

and

$$b_n = \frac{j_n(mx)\left[xj_n(x)\right]' - j_n(x)\left[mxj_n(mx)\right]'}{j_n(mx)\left[xh_n(x)\right]' - h_n(x)\left[mxj_n(mx)\right]'} \tag{2.3}.$$

The coefficient equations for the field inside the sphere are expressed by c_n and d_n, respectively. The scattered field coefficients for the field inside the sphere are expressed as;

$$c_n = \frac{j_n(x)[xh_n(x)]' - h_n(x)[xj_n(x)]'}{j_n(mx)[xh_n(x)]' - h_n(x)[mxj_n(mx)]'} \quad (2.4).$$

and

$$d_n = \frac{mj_n(x)[xh_n(x)]' - mh_n(x)[mxj_n(x)]'}{m^2 j_n(mx)[xh_n(x)]' - h_n(x)[mxj_n(mx)]'} \quad (2.5).$$

In the equations 2.2, 2.3, 2.4, and 2.5 x stands for size parameter ($x = 2\pi n_1 a/\lambda$), where a is the radius of the sphere, λ the wavelength of the electromagnetic wave, m is the relative refractive index ($m = n_2/n_1$), j_n the spherical Bessel function, and h_n the spherical Hankel function [22]. The prime indicates the derivative of the function with respect to the argument [23]. Morphology dependent resonances (MDR's) are observed for the poles of the coefficient functions [24]. The successive values of λ, that minimize the denominator of the equation, continue with a spectral periodicity, which is called mode spacing. These resonances cause extremely high amplitudes of light, resonating in specific discrete wavelengths.

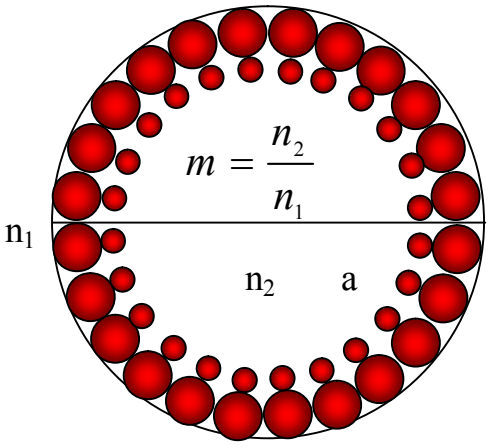

Figure 2.2 A representation of the internal intensity distribution of a microsphere for an MDR with $n = 12$ and $l = 2$.

An MDR is defined by three mode numbers; the polar mode number (*n*), the azimuthal mode number (*m*), and the radial mode number (*l*). The polar mode number defines the number of intensity peaks around the perimeter of sphere; the radial mode number expresses the number of intensity peaks in the radial direction as shown in Fig. 2.2. The azimuthal mode number indicates the great circle, where the photons resonate. However, azimuthal mode numbers are degenerate for a perfect sphere with a degeneracy of 2n+1.

2.3. General Lorenz-Mie Theory

In "special" Lorenz-Mie theory, the Helmholtz equation is solved using spherical symmetry for incoming plane waves. The general Lorenz-Mie theory (GLMT) gives the scattered field of a transversely localized incoming beam, such as Gaussian beam of a laser, from a spherical particle larger than the wavelength of light. The field is expressed by an infinite series of spherical multipole partial waves with specified coefficients [25],

$$b_{nm} = b_n B_n^m \tag{2.6},$$

where

$$B_n^m = \frac{a^2}{n(n+1)\psi_n(x)} \int_0^{4\pi} d\Omega H_r(\Omega) Y_{nm}^*(\Omega) \tag{2.7},$$

where $Y_{nm}^*(\Omega)$ are the spherical harmonic functions, $\Psi_n(x)$ the Ricatti-Bessel function, and $H_r(\Omega)$'s the radial component of magnetic field incident on the surface of the sphere. B_n^m's are the coefficients that define the shape of the beam. GLMT uses these beam shape coefficients, which makes the excitation efficiency position-dependent [26].

2.4 Properties of the Morphology Dependent Resonances

In this section, some important properties of morphology dependent resonances, such as mode spacing, polarization dependence, and quality factor are explained.

2.4.1 The Intrapolarization Mode Spacing

Mode spacing is the separation between resonances with the same radial mode numbers (l) and consecutive polar mode numbers (n). The interpolarization mode spacing is expressed by the equation [27],

$$\Delta\lambda = \frac{\lambda^2 \arctan\sqrt{m^2-1}}{2\pi a n_1 \sqrt{m^2-1}} \qquad (2.8),$$

for a sphere with radius a and relative refractive index m.

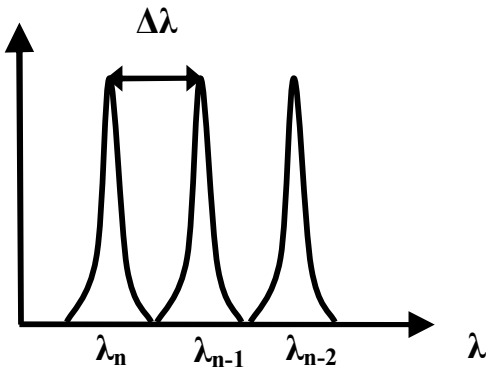

Figure 2.3 Schematic illustration of the intrapolarization mode spacing.

2.4.2 The Interpolarization Mode Spacing

Resonances of TM and TE modes with same polar (*n*) and radial (*l*) mode numbers also have a mode spacing, which can be expressed as [28];

$$\Delta\lambda_p = \frac{\lambda^2 \arctan\sqrt{m^2 - 1}}{2\pi a n_2} \tag{2.9},$$

for a sphere with radius a and relative refractive index m.

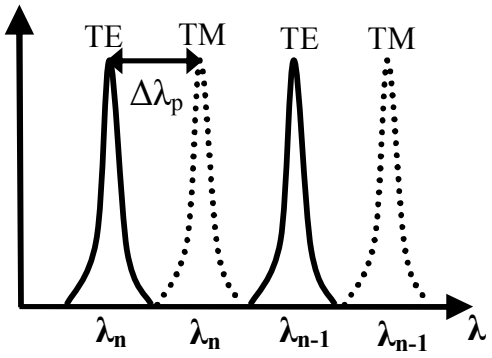

Figure 2.4 Mode spacing of nearly identical TE and TM resonances.

While intrapolarization mode spacing is not relatively very sensitive to n_1, the interpolarization mode spacing is strongly sensitive to n_1. The interpolarization mode spacing of nearly identical TE and TM modes is used for refractive index sensing [15].

2.4.3 The Quality Factor

The quality factor of an optical resonator defines how long a photon stays resonating inside the cavity [29]. A very common way to introduce the quality factor of a resonator, that keeps photons inside for a lifetime of τ, is,

$$Q = \frac{\omega_0}{\Delta\omega_{1/2}} = \omega_0 \tau \qquad (2.10),$$

where $\Delta\omega_{1/2}$ is the full width half maximum of the resonance.

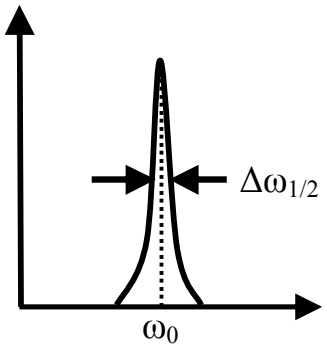

Figure 2.5 Identifying of the quality factor of a resonance peak.

Another explanation for the quality factor is in terms of the stored photonic energy inside the optical resonator. Eq. 2.11 expresses the quality factor of a resonator in terms of energy.

$$Q = 2\pi \frac{stored \quad energy}{energy \quad loss \quad per \quad cycle} \qquad (2.11).$$

Energy loss for an optical resonator can be accounted by four channels; radiative (curvature) losses (Q_{rad}), absorption losses (Q_{abs}), scattering losses (Q_s) and surface contaminant losses (Q_{cont}).

$$\frac{1}{Q} = \frac{1}{Q_{rad}} + \frac{1}{Q_{abs}} + \frac{1}{Q_s} + \frac{1}{Q_{cont}} \tag{2.12}$$

Radiative loss is the escape of photons through the effective potential barrier [20]. The smaller the microsphere, the higher the number photons escaping through the cavity. Absorption loss is due to change of photon energy to heat energy. Absorption loss is due to transformation of electromagnetic energy to heat by non-radiative decay of photons. Scattering losses are caused by the molecular size surface inhomogeneities. Scattering loss is not different than Rayleigh scattering. Surface contaminant losses depend on the fabrication process of the microspheres such as adsorption of water molecules on the surface or the dirt on the surface of the microsphere [30].

In addition to the loss processes explained, one more loss mechanism occurs for waveguide coupled microsphere systems. Q_e, identified as the coupling loss accounts as an external loss factor. The total quality factor can be expressed by the Eq. 2.13 [31].

$$\frac{1}{Q_{total}} = \frac{1}{Q} + \frac{1}{Q_e} \tag{2.13}$$

The quality factor of a resonator is an important factor in the development of devices with extremely high sensitivities.

2.5 Coupling to the Resonances

Practical applications of microsphere resonators pose the important problem of efficient and controllable coupling of light into the microspheres. Morphology dependent resonances are observed, when the evanescent field of coupler and the microsphere overlap and phase-matching conditions are satisfied [32]. The efficiency of excitation of MDR's depends on the distance between the beam waist and the center of the microsphere. The distance between the beam waist and the center of the microsphere is called the "impact parameter", described by **b**. The impact parameter should obey Eq. 2.14 for excitation of the MDR's [20].

$$a \leq b \leq ma \tag{2.14},$$

where a is the radius, and m the relative refractive index of the microsphere.

2.5.1 Coupling Techniques

Many techniques are developed for evanescent wave coupling to MDRs of microspheres, as shown in the following figure [33].

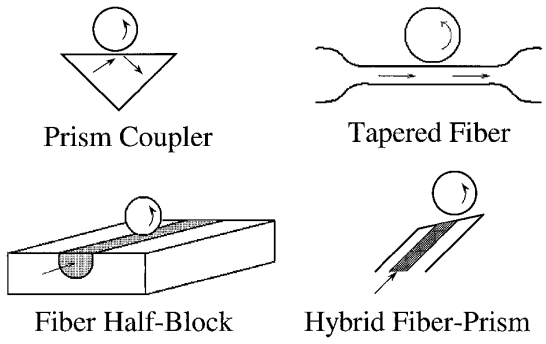

Figure 2.6 Evanescent wave coupling techniques to the microspheres.

Prism coupling is relatively easy method and tunable. Tapered fiber method is also a quite easy method, but the thickness of the tapered fiber has to be around 5 μm, and fiber is very fragile at this thickness. Hybrid fiber-prism coupling uses the advantages of prism coupling and fiber coupling. Optical fiber half coupling looks like the most promising coupling method for optical integration.

2.5.2 Optical Fiber Half Coupler

An optical fiber half coupler (OFHC) is fabricated by burying the fiber in a glass block and polishing the single mode fiber until a couple of micrometer distance is left to the core. In Fig. 2.8, the coupling geometry from the OFHC to the microsphere is shown. Since the nearest region of the fiber core to the surface is the middle of the OFHC, the most efficient coupling is expected, when the microsphere is at the center of the OFHC.

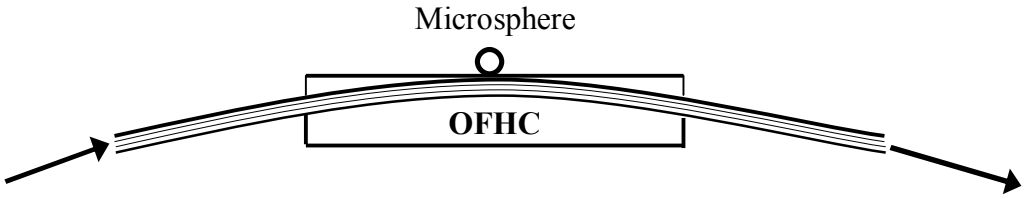

Figure 2.7 Coupling geometry of light to the microsphere.

The OFHC used in the experiments is a single mode OFHC in 630 nm region with a core refractive index of 1.47 and cladding refractive index of 1.45. The diameter of the core is approximately 4 micrometers. The diameter of the cladding is 125 μm.

Chapter 3

NEMATIC LIQUID CRYSTALS

3.1 Introduction

Crystals are structures, that are formed by atoms and molecules sustaining an order in space. The centers of gravity of conventional cells are ordered in crystals, whereas they are not ordered in amorphous materials [41]. A phase of matter exists, different than a solid such as a crystal or a liquid, called liquid crystal. Liquid crystals (LC's) are materials, that show liquid properties such as viscosity and solid properties such as ordered structure. Although LC molecules act like liquids in most of the cases, they implement some degree of orientational order, even sometimes positional order.

The simplest liquid crystal phase named "nematic phase" shows orientational order. One molecular axis prefers to orient to a specific direction as the molecules undergo diffusion. The preferred direction is called the director ($\hat{n}$). The orientational distribution function f(θ) can be defined as taking pictures of molecules at any time and checking the number of molecules making an angle θ with the director, or following a molecule and noting specific times that the molecule is at an angle θ with the director. This phase, in which only orientational order exist, is called the nematic phase. A snapshot of molecules in nematic phase is represented in Fig. 3.1. The orientational order parameter S can be expressed by the angle average of second Legendre polynomial, $P_2(\cos\theta)$,

$$S = \langle P_2(\cos\theta) \rangle = \left\langle \frac{3}{2}\cos^2\theta - \frac{1}{2} \right\rangle \qquad (3.1),$$

where brackets present the angle average of many molecules or the time average of one molecule [42].

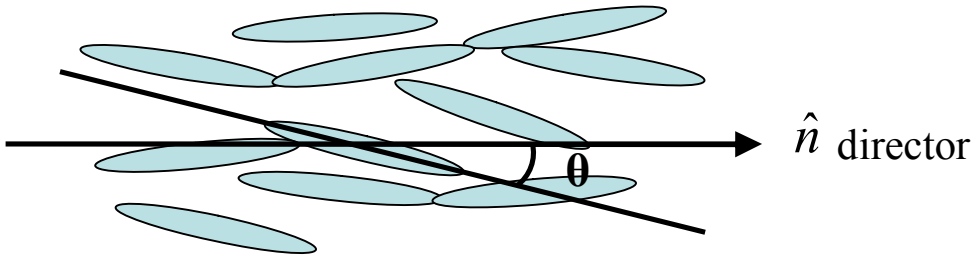

Figure 3.1 Molecular order in a nematic liquid crystal.

3.2 Structural Properties of Nematic Liquid Crystals

Liquid crystals are generally rod shaped, long molecules. There are also disk shaped nematic liquid crystals, which have fewer applications. Only, rod shaped nematic liquid crystals are introduced and discussed in this chapter.

Hans Kekler synthesized the first room temperature nematic liquid crystal, N-(4-Methoxybenzylidene)-4-butylaniline (MBBA) in 1969 [43].

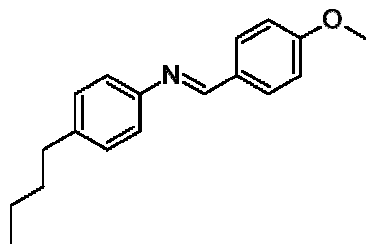

Figure 3.2 Chemical structure of the MBBA.

In 1972, another room temperature nematic liquid crystal, which is very common in display technologies, and known as 4-Cyano-4'-pentylbiphenyl (5CB) is synthesized [44]. 5CB was the first member of cyanobiphenyls. E7 is a mixture of cyanobiphenyls which is used for liquid crystal displays (LCDs).

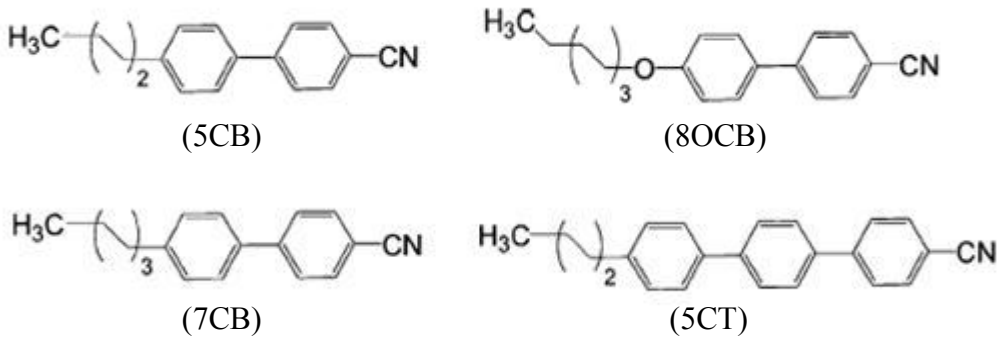

Figure 3.3 Chemical structures of the cyanobiphenyls used in the E7 mixture.

E7 consists of 50.6% of 4-pentyl-4'-cyanobiphenyl (5CB), 25.2% of 4-heptyl-4'-cyanobiphenyl (7CB), 17.8% of (c) 4-octyloxy-4'-cyanobiphenyl (8OCB), and 6.4% of 4-pentyl-4'-cyanoterphenyl (5CT) with a clearing point of about 58 °C [45]. However, the clearing point of 5CB, which is one of the molecules used in E7 mixture, is 38 °C. Mixtures are developed for the broad nematic phase temperature interval.

Cyanobiphenyls are liquid crystalline molecules with hydrophilic polar head, and hydrophobic non-polar tail. This property gives them self-assembling properties inside water or hydrophobic liquids.

Figure 3.4 Hydrophilic head and hydrophobic tail of an LC molecule.

Micelles and reverse micelles are structures, that molecules with a hydrophilic head and hydrophobic tail form. In Fig. 3.5, a micelle inside water and a reverse micelle inside a hydrocarbon liquid are shown.

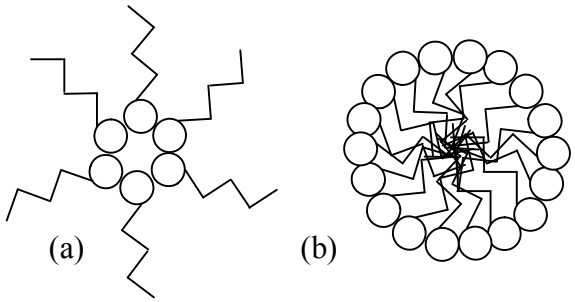

Figure 3.5 Illustration of (a) reverse micelle and (b) micelle.

Liquid crystals can be placed in a cell and aligned to a direction for optical switching, modulation or display purposes. This causes three types of deformations, which are bend (B), splay (S), and twist (T) deformations [46].

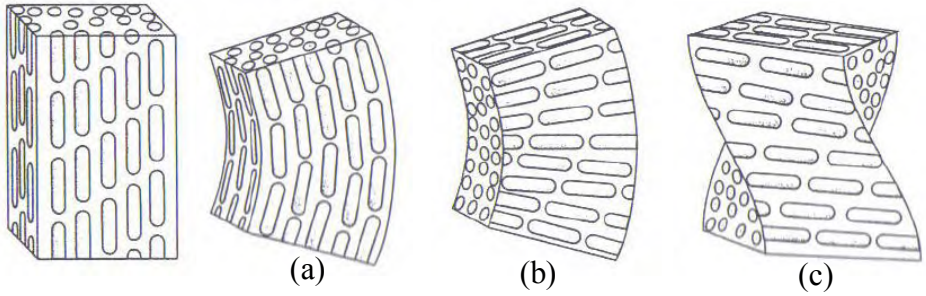

Figure 3.6 Illustration of (a) bend, (b) splay, and (c) twist deformations [46].

Free volume elastic energy (Frank's energy) density of liquid crystal can be expressed as,

$$g = \frac{1}{2}\left[K_{11}(\vec{\nabla}.\hat{n})^2 + K_{22}\left[\hat{n}.(\vec{\nabla}\times\hat{n})\right]^2 + K_{33}\left|\hat{n}\times(\vec{\nabla}\times\hat{n})\right|^2 \right] \qquad (3.2),$$

where K_{11} is the splay deformation constant, K_{22} the twist deformation constant, and K_{33} the bend deformation constant.

3.3 Optical Properties of Nematic Liquid Crystals

As the liquid crystal molecules are anisotropic in shape, their optical properties are also anisotropic. They have two different refractive indices for two different axes. This property is called birefringence. Two different types of birefringence exist; positive birefringence and negative birefringence.

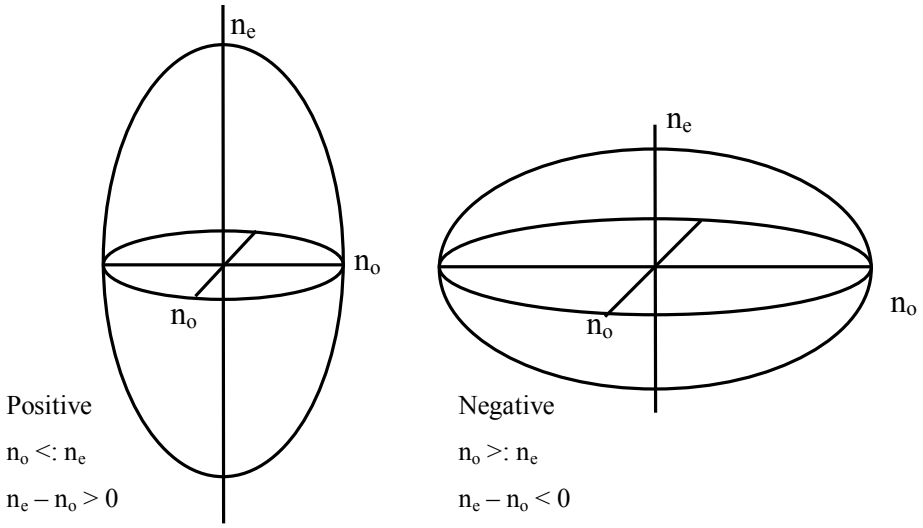

Figure 3.7 Positive and negative birefringence.

If the refractive index of the extraordinary axis is larger than the ordinary axis, it means the molecule is positively birefringent. However, if the refractive index of the ordinary axis is larger, the molecule is negatively birefringent. In our experiments, we used 5CB, which is a positively birefringent nematic LC. Positively birefringent LC has one preferred reoritentation direction under external electric field. On the other hand, negatively birefringent LC has two preferred reorientation direction under the external electric field, which causes instability on the reorientation of the liquid crystal. The ordinary refractive index of 5CB is 1.53452 and the extraordinary refractive index is 1.71182 [47].

The refractive index of an LC molecule for polarized light can be expressed by the following equation [48],

$$n(\theta_p) = \frac{n_e}{\sqrt{\cos^2\theta_p + \frac{n_e^2}{n_o^2}\sin^2\theta_p}} \qquad (3.1),$$

where n_e is the extraordinary refractive index, n_o the ordinary refractive index and θ_p the angle between extraordinary axis of the molecule and the polarization of light wave.

3.4 Electroptical Properties of Nematic Liquid Crystals

By using the polar property of liquid crystal molecules, it is possible to control their orientation by an external electric field. If an external electric field is applied to the LC, the director of the molecule orients itself paralel to the applied electric field.

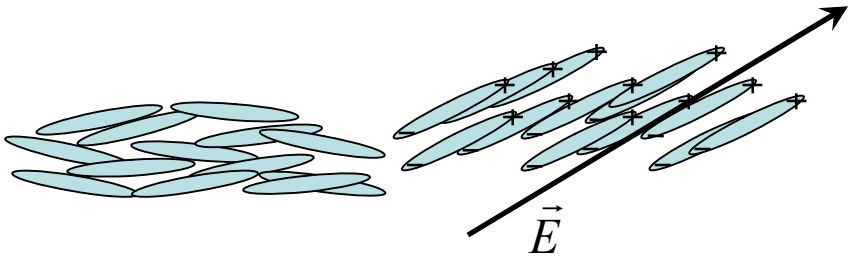

Figure 3.8 LC alignment by external electric field $\vec{E}$.

The twisted nematic cell is a very efficient way to control the birefringence by means of an applied voltage. The twisted nematic cell is a liquid crystal sandwich between two glasses and two orthogonal polarizers. LC molecules are aligned in orthogonal direction at the opposite glass boundaries. When the planar orientation of nematic liquid crystals are orthogonal to each other in opposite electrodes of a nematic LC cell, the applied electric

field along the z direction generates reorientation of molecules with a combination of bend, splay and twist deformations [49]. The threshold voltage for reorientation of the LC molecules can be expressed as,

$$V_{tw} = \sqrt{\pi^3 \Delta\varepsilon^{-1}\left(4K_{11} + K_{33} - 2K_{22}\right)} \qquad (3.2),$$

where $\Delta(1/\varepsilon)$ represents the change in the permittivity of the LC before and after the reoritentation.

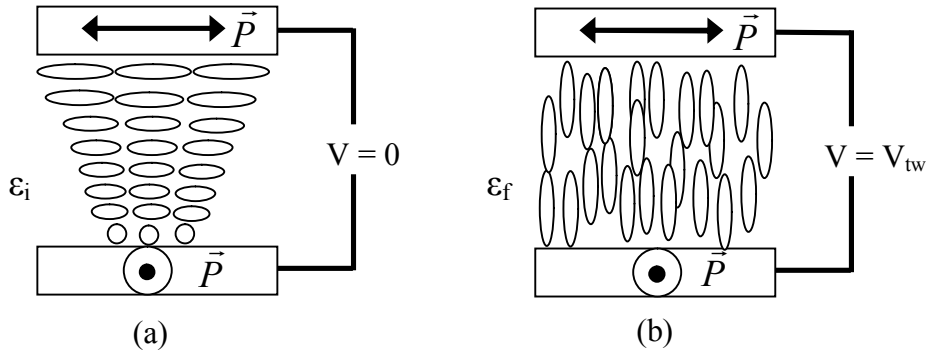

Figure 3.9 The orientation of LC in a twisted nematic cell, when (a) no voltage is applied and when (b) the threshold voltage is applied.

In Fig. 3.9 a representation of twisted nematic cell is shown. $\vec{P}$ represents the polarizers on the glass slides. When there is no voltage applied, the twisted cell act as a half wave plate, which allows light transmission through the cell. When the threshold voltage is reached, the LC molecules reorient and the twisted cell does not act like a half wave plate, and results in no light transmission through the cell.

Chapter 4

ELASTIC LIGHT SCATTERING FROM GLASS MICROSPHERES IN FLUIDS

4.1 Experimental Setup

In this chapter, the results of the experiments with titania nanoparticle doped high refractive index glass microspheres are reported. Microspheres with diameters of 23 μm, 55 μm, and 103 μm and refractive index of 1.9 are used in the experiments. In the first part, the relation between the impact parameter and the spectra of microspheres are explained and demonstrated in high refractive index microspheres with diameter of 103 μm experimentally. In the second part, the spectra of high refractive index microspheres with diameters of 23 μm and 55 μm is showed in two different (TE and TM) polarizations. In the last part, experimental results in amorphous and crystalline liquids are shown and the results are discussed.

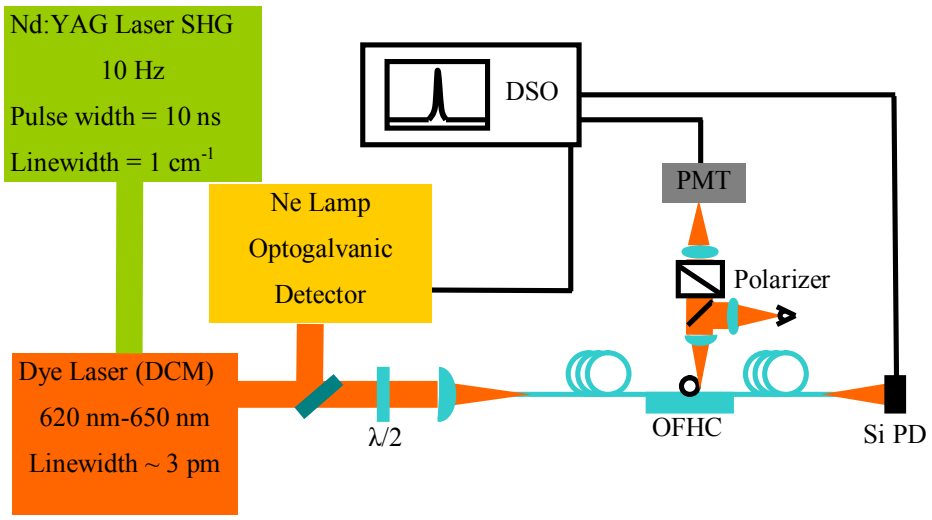

Figure 4.1 The schematic of the experimental setup.

As shown in Fig. 4.1, the Nd:YAG pumped dye laser is used to obtain spectra. The laser input light is focused to a single mode optical fiber (SMOF) at 630 nm. The 90°

elastic light scattering is detected by a photomultiplier tube (PMT). The transmission is measured by a silicon photodiode (PD); however there are no dips observed in the transmission because of the weak coupling of resonances into the microsphere. All the data are recorded using a digital storage oscilloscope (DSO).

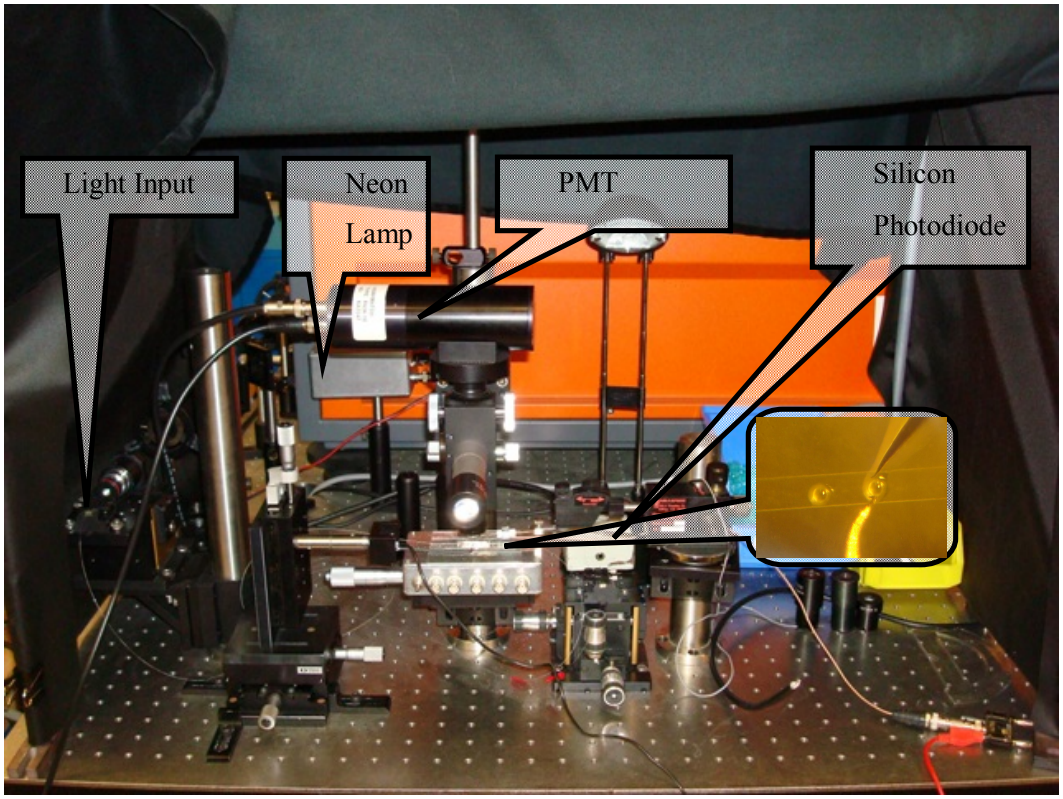

Figure 4.2 Picture of the experimental setup.

In the experiments, microspheres with diameters of 23 μm, 55 μm, and 103 μm are used. The input polarization of light into the fiber is tuned by an achromatic half wave (λ/2) plate before the fiber coupling. A Glan polarizer is placed in the objective to perform better polarization selection of 90° scattering.

In Fig. 4.9, two titania nanoparticle doped high refractive index microspheres with diameter of 55 μm are shown. The microspheres are positioned by using a micropositioner with a tungsten tip of diameter 10 μm.

The coupling geometry is the same for all the experiments, that are discussed in this section. Microspheres are placed on a single mode optical fiber half coupler (OFHC). The optical resonances are coupled to the microspheres by evanescent wave coupling from the OFHC.

4.2 Properties of the Light Source

4.2.1 Nd:YAG Laser

Laser is a device that produces identical photons, having the same phase and frequency, by stimulated emission of radiation. The first laser is operated on 16 May 1960 at the Hughes Research Laboratories in Malibu, California, USA. This was a ruby laser optically pumped by flash lamps. After the operation of the first laser, various kinds of lasers are developed with a huge variety of materials. Generally lasers can be classified as solid state, gas, liquid and semiconductor lasers according to their gain material. In the experiments, a Nd:YAG (Neodymium doped Yttrium Aluminum Garnet) laser by Spectra Physics is used to pump the dye laser by Lambda Physik.

The Nd:YAG laser is a Q-switched pulsed laser, that has minimum pulse duration time of 10 ns and a repetition rate of 10 Hz. The maximum power output of the laser is 1 J/pulse. Nd: YAG laser gives light at 1064 nm. In addition to the fundamental wavelength, the second harmonic generation (SHG) at 532 nm and the third harmonic generation (THG) at 355 nm are generated by two KDP (Potassium Dideuterium Phosphate) crystals. The laser beam is multimode Gaussian shaped and has approximately 10 mm diameter. The spectral linewidth of the laser is 1 cm^{-1}. The SHG at 532 nm is used to pump the dye laser.

4.2.2 The Dye Laser

Dye lasers are optically pumped light sources using an organic dye solution as a gain material. Dye lasers have great applications for their broad emission spectrum, leading to broad tuning ranges. In Fig. 4.3, the optical schematic of the dye laser by Lambda Physik used in the experiments is shown.

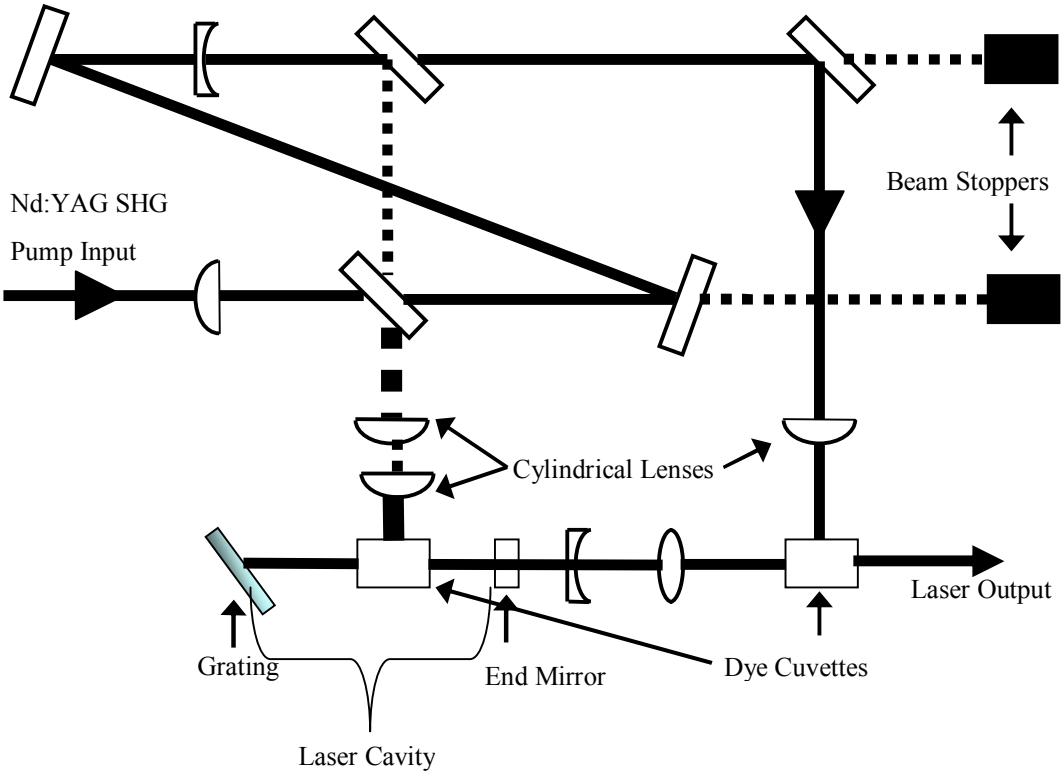

Figure 4.3 Schematic of the dye laser optics.

The laser has two cuvettes with a dye solution flowing inside. The first cuvette is inside the cavity of the laser for laser oscillation and pre-amplification. The second cuvette is for amplification of the laser output power. The output wavelength of the dye laser is tuned by controlling the angle of the grating by a stepper motor.

4.3 Optogalvanic Effect for Dye Laser Wavelength Calibration

The change in the electrical properties of a plasma, when illuminated with a light source with a frequency corresponding to an atomic or molecular transition of the plasma, is called optogalvanic effect [34]. The optogalvanic (OG) effect is discovered by Penning in 1928. The optogalvanic effect has been used for laser calibration with the atomic lamps. Previous works show that, the wavelengths and the relative intensities of the spectral lines measured with OG technique, using CW laser are in good agreement with the emissions [35, 36]. In addition, OG effect is used for pulsed dye laser calibration with a resolution of the laser linewidth [37].

In our experiment, our pulsed dye laser is calibrated using a commercial neon lamp. Optogalvanic neon signal is observed during the whole dye laser spectrum [38].

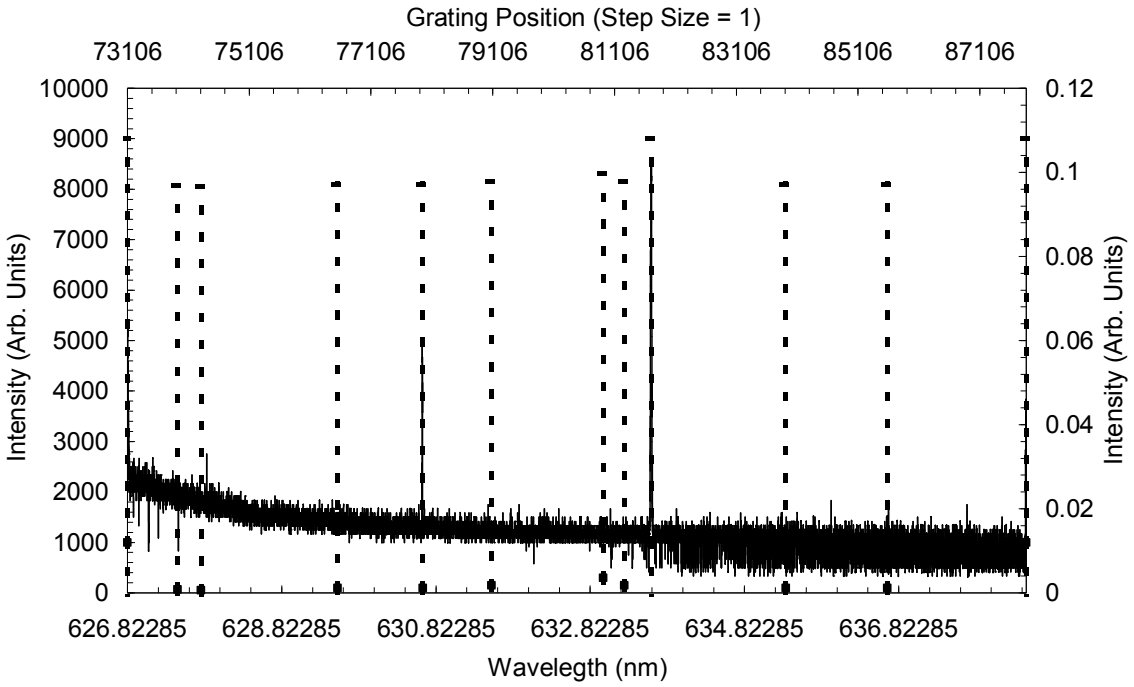

Figure 4.4 Matching of Ne spectral lines with optogalvanic neon signal.

In Fig. 4.4, the Ne transitions are the dashed lines. The optogalvanic Ne transitions are observed for the wavelengths of 627.5668 nm, 631.4268, 634.4388 nm, and 639.3636 nm in the optogalvanic signal.

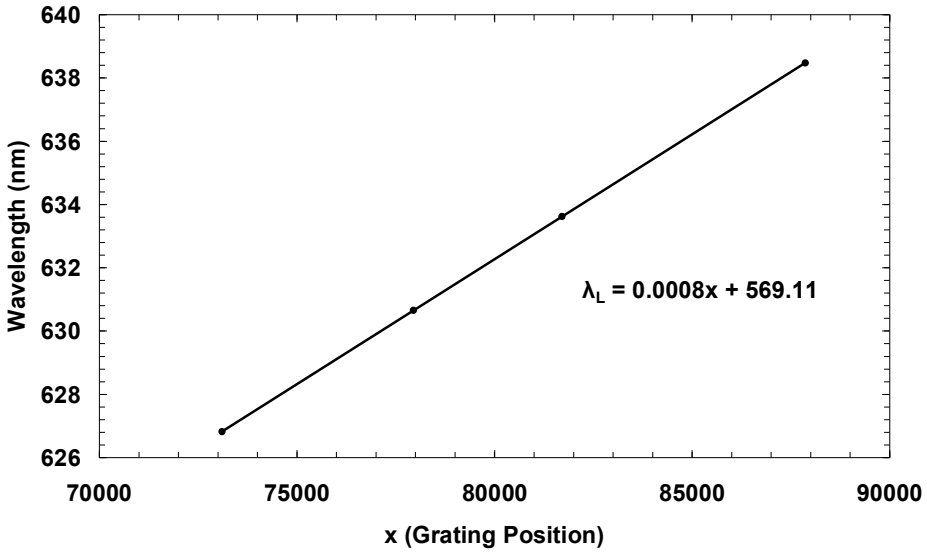

Figure 4.5 The Wavelength calibration line of dye laser.

In Fig. 4.5, the wavelength calibration line of dye laser is shown. The equation for finding the wavelength corresponding to a grating position is found using the following equation;

$$\lambda_L = 0.0008x + \lambda_0. \quad (4.1),$$

where, λ_L is the wavelength of the dye laser, x the grating position, and λ_0 the wavelength for the original position of the grating.

4.4 The Dye Gain Curve

The tuning range of the dye laser is found (as seen in Fig. 4.4) after the wavelength calibration. The dye laser has a tuning region between 615 nm and 655 nm. The output intensity of the dye laser is measured using a Si photodiode (PD). The background signal comes from the other sources in the environment.

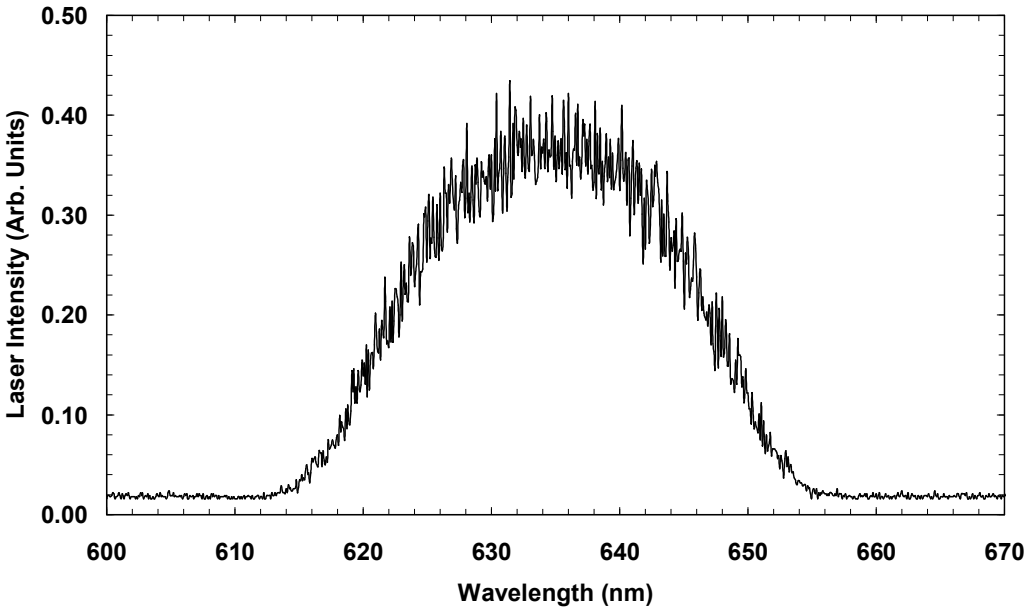

Figure 4.6 The dye laser tuning curve.

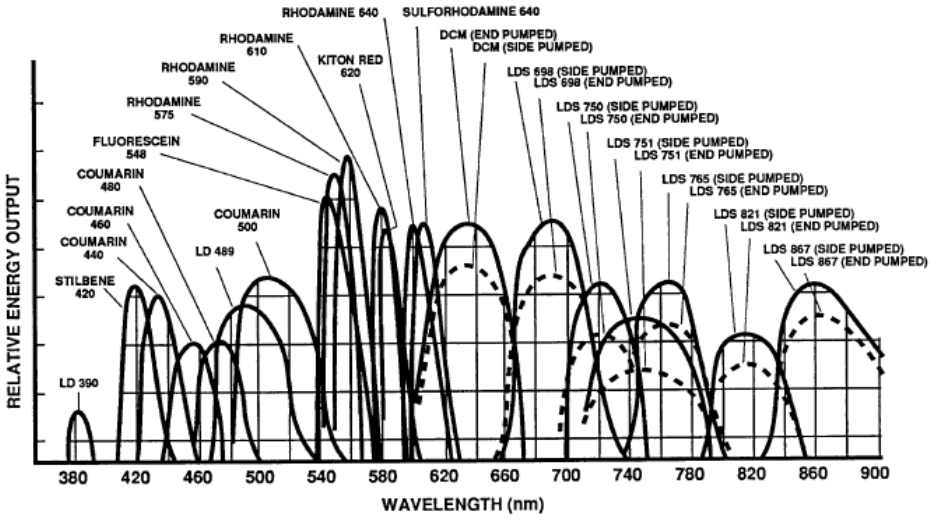

Figure 4.7 Dye emission spectra [39].

The dye we used for our experiment is [2-[2-[4-(dimethylamino)phenyl]ethenyl]-6-methyl-4H- pyran-4-ylidene]-propanedinitrile (DCM).

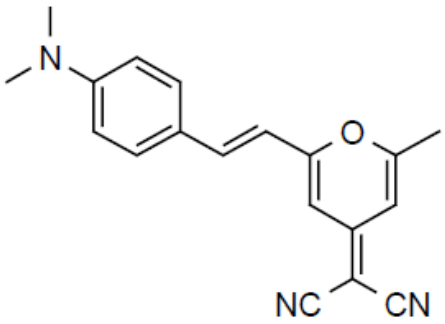

Figure 4.8 Chemical structure of the DCM.

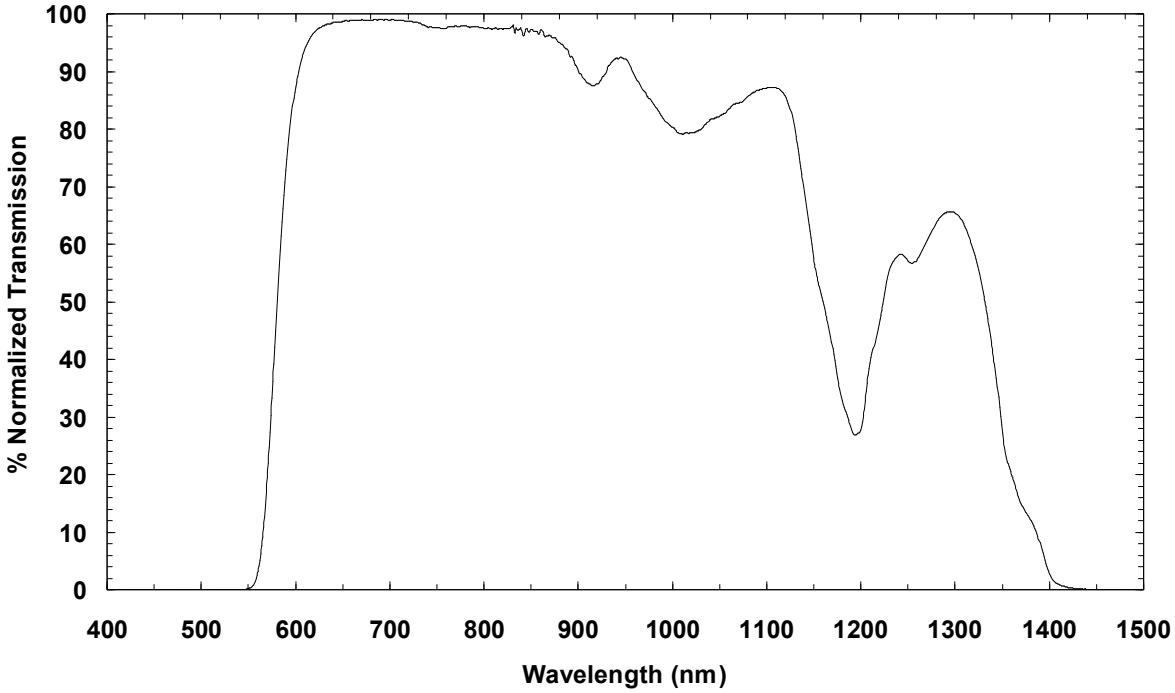

Figure 4.9 Transmission spectrum of the DCM dye solution.

The transmission spectrum of the DCM dye is taken between 400 nm and 1500 nm by a UV-visible spectrophotometer. The measured dye is in a solution of ethanol placed inside a quartz cuvette. Absorption is observed at wavelengths smaller than 550 nm as expected. 532 nm is the pump wavelength and 615 nm – 655 nm is the lasing wavelength region of the dye.

4.5 Elastic Light Scattering from Microspheres in Air

4.5.1 Impact Parameter Dependence of Resonances

The coupling of light power to the resonator can be expressed by the Eq. 4.2.

$$|\kappa|^2 = 1 - |t|^2 \tag{4.2}.$$

where, κ is the field coupling coefficient and t the field transmission coefficient. The coupling coefficient is inversely proportional to the impact parameter (**b**) [40].

In this experiment, the microsphere position on the OFHC is determined for the most efficient coupling. As shown in the Fig. 4.10, if the microsphere is not at the center of the optical fiber, an azimuthal mode number different than zero is excited and the impact parameter (b) increases.

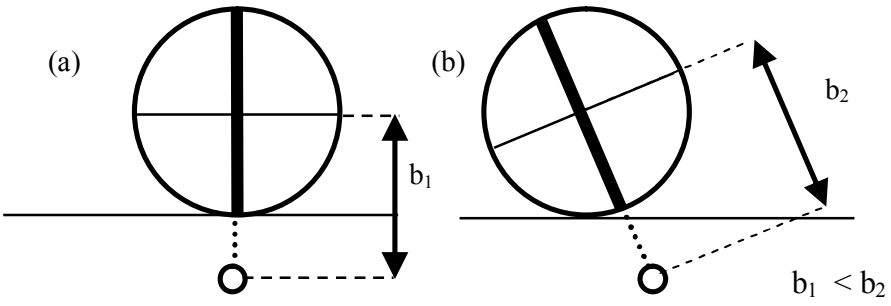

Figure 4.10 Front view of microsphere – optical fiber coupling geometry.

Thick lines on the sphere are the pathway of the resonating photons in figure 4.10. The microsphere position in Fig. 4.10 and the corresponding schematic spectra in Fig. 4.11 represent (a) when microsphere is at the center of optical fiber, and (b) when the microsphere is not at the center of the optical fiber.

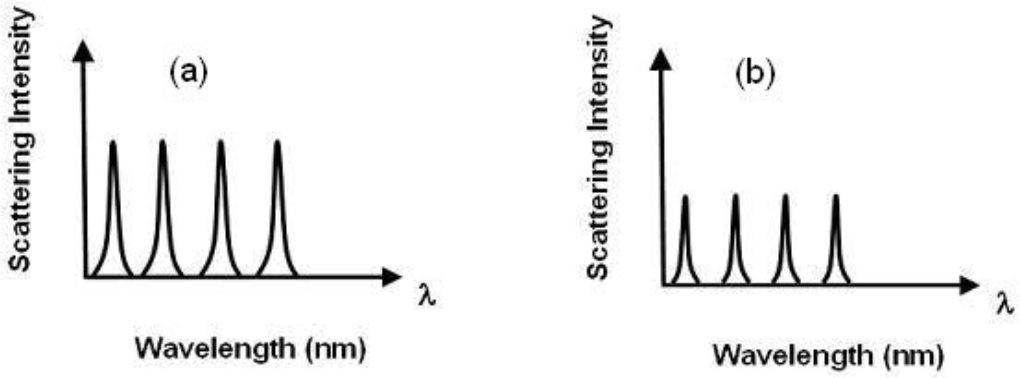

Figure 4.11 Schematic of microsphere spectra for two different positions on the OFHC.

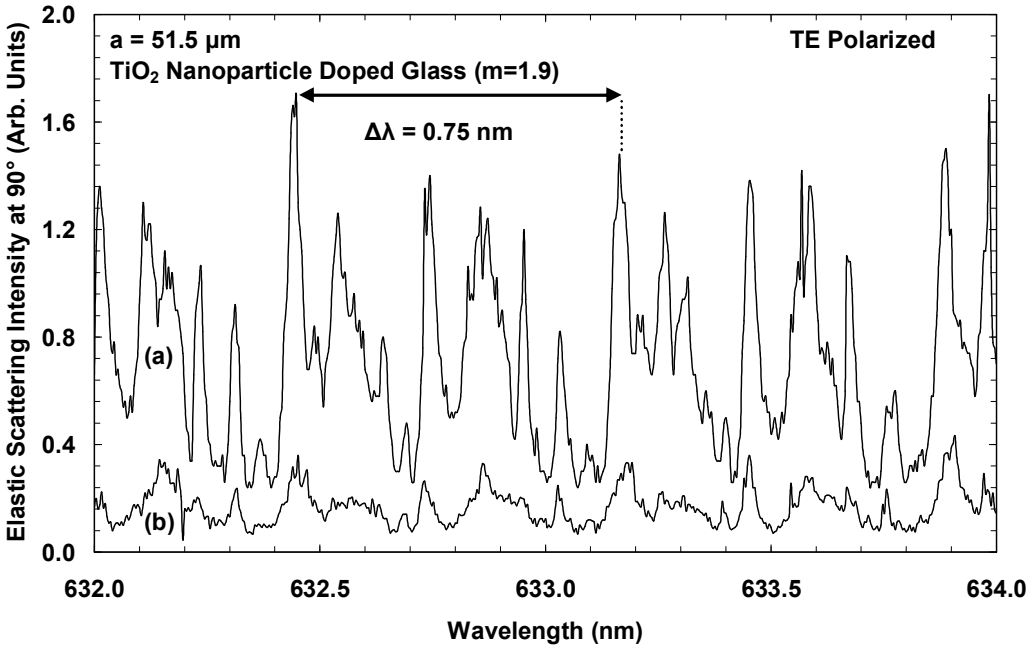

Figure 4.12 Microsphere spectra for two different positions on the OFHC.

In Fig. 4.12, the experimental result is shown with two different microsphere positions of the same microsphere on optical fiber. The position of the microsphere is changed by the tungsten probes. In Fig. 4.12 (a), the microsphere is laterally at the center of the fiber. In Fig. 4.12 (b), the microsphere is not laterally at the center of the fiber. The two spectra are similar except the intensities. Thus, the impact parameter only affects the coupling coefficient in the experiments. The mode spacing is found to be 0.75 nm for microspheres with diameter of 103 μm. The mode spacing and the quality factor remain the same in both spectra. Resonance modes, existing inside the mode spacing region, are other radial resonance modes corresponding to different *l* values.

4.5.2 The Polarization Dependence of Resonances

The polarization direction is the electric field oscillation direction of an electromagnetic wave. The definition of refractive index comes from the total dipoles, that are found in a unit volume of a material. The interaction direction of the electromagnetic wave with the dipoles depends on the polarization direction of the electromagnetic waves. Therefore, a difference in refractive index and penetration depth comes about with respect to two different polarizations at the interfaces. This leads to different resonant frequencies for TE and TM modes, even when all mode numbers are the same for both polarizations.

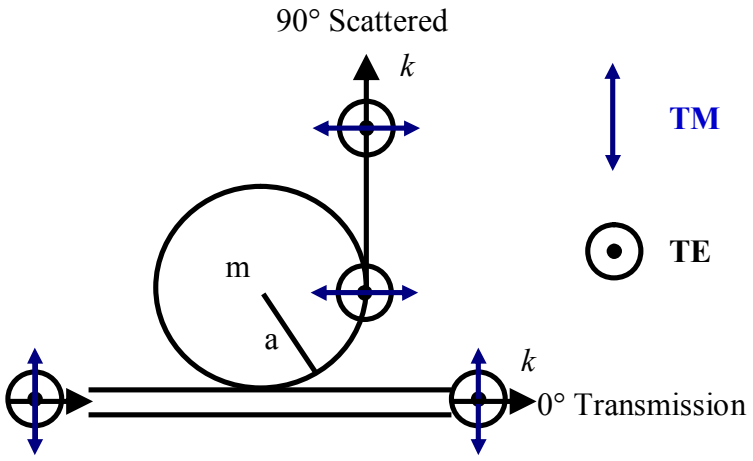

Figure 4.13 The illustration of TE and TM modes in the waveguide and the microsphere.

Different resonance frequencies for two polarizations imply different optical pathways. The graphical representation of TE and TM modes is illustrated in Fig. 4.13.

In Fig. 4.14, elastic light scattering spectra of a microsphere at 90° with diameter of 55 μm is presented. The mode spacing is measured as 1.18 nm for both TE and TM polarizations and calculated as 1.42 nm by Eq. 2.8. The error is found as 17% for the mode spacing. A TE-TM mode spacing of 0.9 nm is measured and calculated as 1.01 nm (Eq. 2.9) for a microsphere with a diameter of 55 μm. A 10% of error is found for $\Delta\lambda_p$ for the microsphere with a diameter of 55 μm.

In Fig. 4.15, the elastic light scattering spectrum of the same microsphere with 55 μm diameter is measured, when both TE and TM polarizations are coupled to the microsphere. The measured spectrum looks like the addition of TE and TM intensities in Fig. 4.14 as expected.

In Fig. 4.16, the elastic light scattering spectra of a microsphere at 90° with a diameter of 23 μm is presented. The mode spacing is measured as 3.23 nm for both TE and TM polarizations. The mode spacing is calculated to be 3.51 nm (Eq. 2.8). The error is 8% for the mode spacing. A TE-TM mode spacing of 2.46 nm is measured, and calculated as 2.49 nm (Eq. 2.9) for a microsphere with a diameter of 23 μm. The differences between the measured and calculated values for $\Delta\lambda_p$ correspond to 1.2%. The deviation probably comes from the size distribution of microspheres, which is in the range of 5%. A diameter of approximately 23.8 μm minimizes the errors for both mode spacing values.

The error found for the microsphere with a diameter of 55 μm is 10 times more than the error of the microsphere with diameter of 23 μm. As the size of the microsphere increases, the number of whispering gallery modes (WGM's) increases, which leads difficulties in the indentification of resonance peaks in the spectrum. One possibility might be merging of resonance peaks, thereby increasing the uncertainty of the resonance peaks corresponding to the same mode numbers of different polarization. A diameter for of 65.7 μm minimizes the error, which might be the actual diameter of the microsphere.

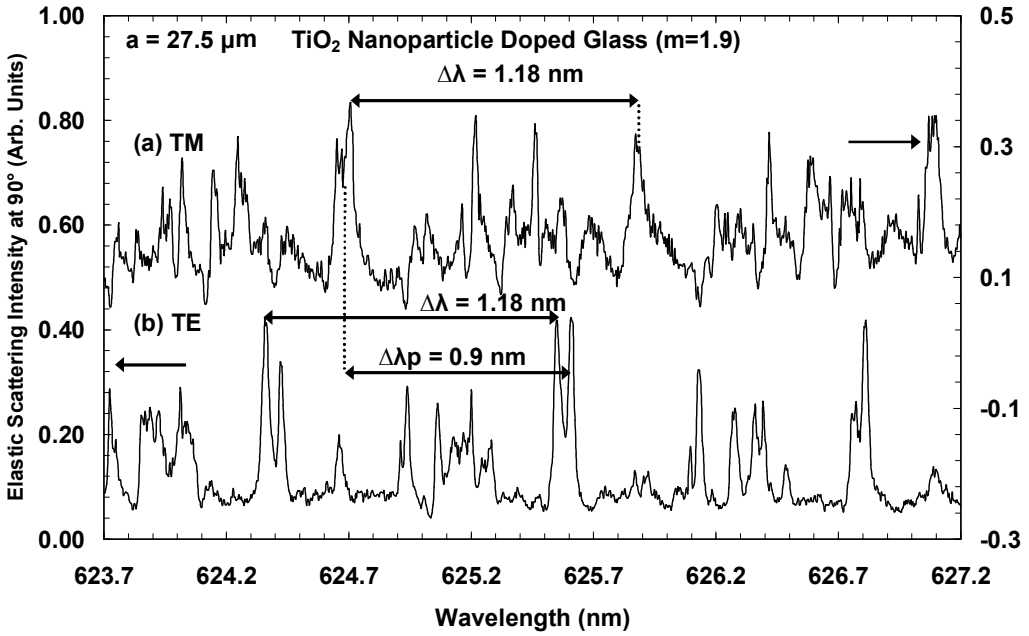

Figure 4.14 Elastic light scattering spectra of a microsphere with diameter of 55 μm at 90° for (a) TM and (b) TE polarizations.

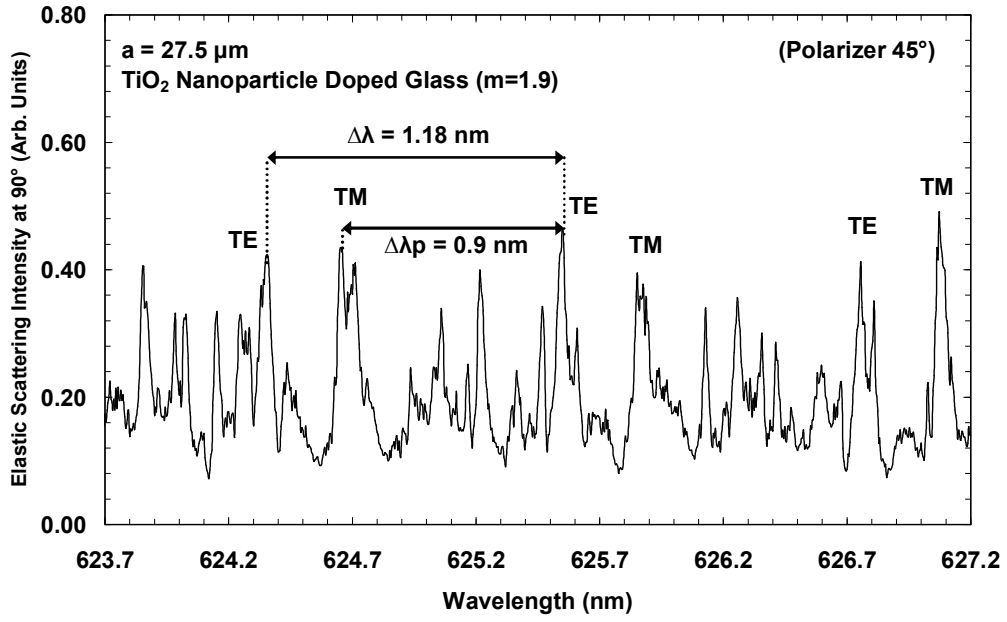

Figure 4.15 Elastic light scattering spectrum of a microsphere with diameter of 55 μm at 90°. for both TE and TM polarizations.

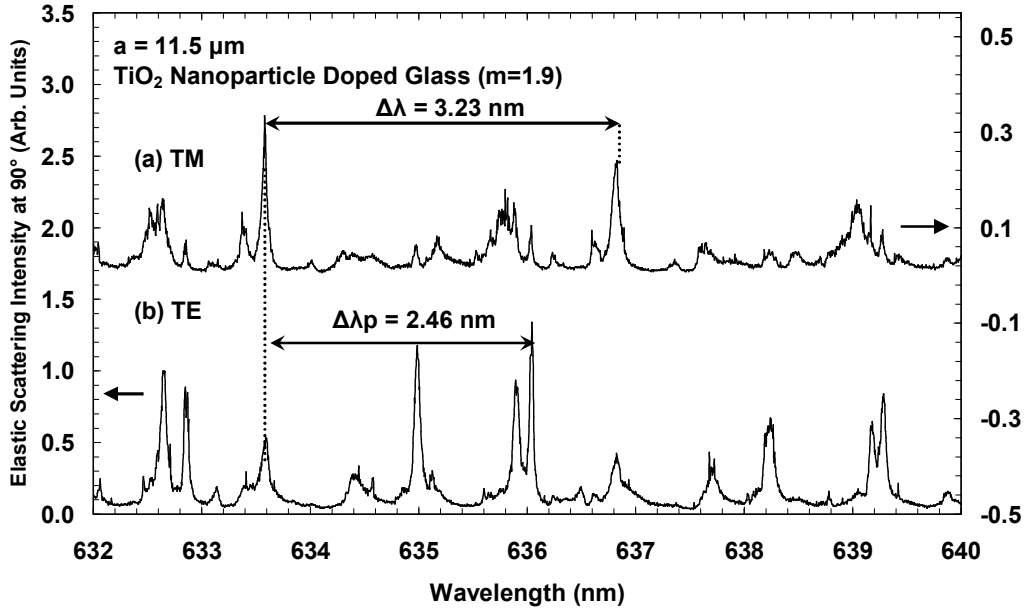

Figure 4.16 Elastic light scattering spectra of a microsphere with diameter of 23 μm at 90° for (a) TM and (b) TE polarizations.

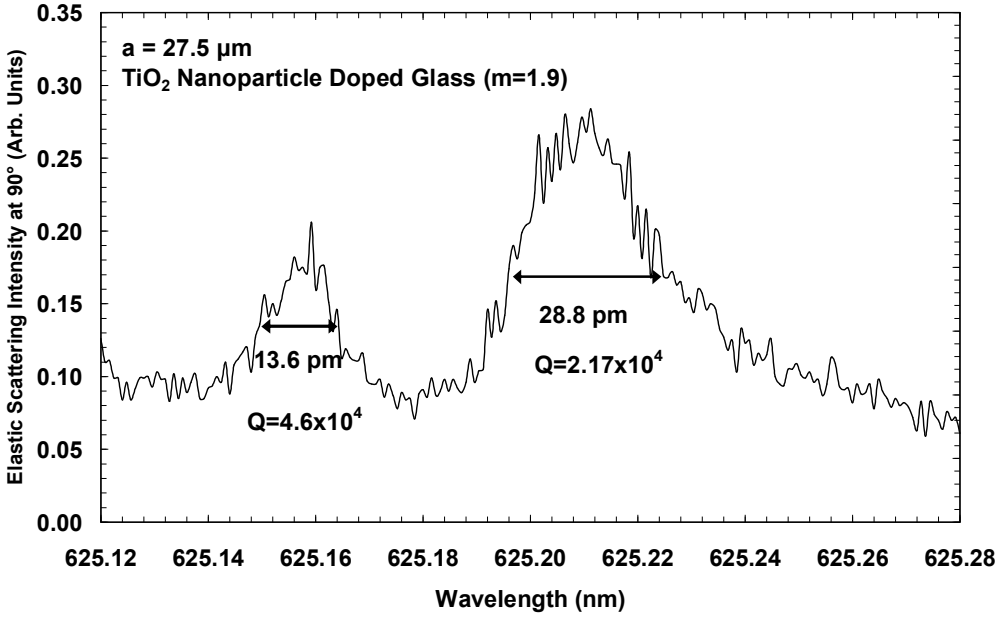

Figure 4.17 High resolution spectrum of two MDR's for Q-factor measurement.

Fig. 4.17 shows the FWHM measurement of two resonance peaks. The quality factors are calculated by the Eq. 2.10 as 4.6×10^4 and 2.2×10^4.

To summarize, the relation of spectra between microsphere position on the optical fiber and polarization of the excitation light is discussed and showed experimentally in this section. A decrease in the elastic light scattering is observed with increasing impact parameter. Then, the TE-TM mode spacing is determined, and used to find the actual size of the microspheres. Finally, the Q-factors of resonances are measured by high resolution spectroscopy of the microspheres.

4.6 Elastic Light Scattering from Microspheres in Amorphous Liquids

The unit particles of a material in liquid phase are weakly interacting, randomly walking atoms or molecules. Since, there is no ordered structure in liquids; they show amorphous behavior with isotropic material properties. The order parameter of a liquid is zero, which can be calculated by Eq. 3.1. In experiments in this section, elastic light scattering from the microspheres inside fluid media is measured at 90°. The spectra of the microspheres inside air, distilled water (H_2O), and glycerol ($C_3H_5(OH)_3$) are measured. The liquids are placed on the OFHC and covered the whole surface of the microspheres. All the measurements are performed for TE polarized scattered light by microspheres with a diameter of 23 μm.

The spectra in Fig. 4.18 and 4.19 are from the same microsphere. The first measurement is done, when the microsphere is inside water (Fig. 4.18 (b)). Secondly, the spectrum is measured after the evaporation of water (Fig. 4.18 (a)). Finally, elastic light scattering spectrum is taken inside glycerol which has a refractive index of 1.47. The mode spacing for all the measurements is 2.95 nm. However, significant differences are observed in Q-factors, and background signals of the spectra. In Fig. 4.8, a slight change in background signal appear. When the microsphere is inside water, more light scatters out of the OFHC than the dry OFHC. This is caused by relatively high refractive index of water (1.3) with respect to air (1). However, there is no considerable change in the Q-factor of re-

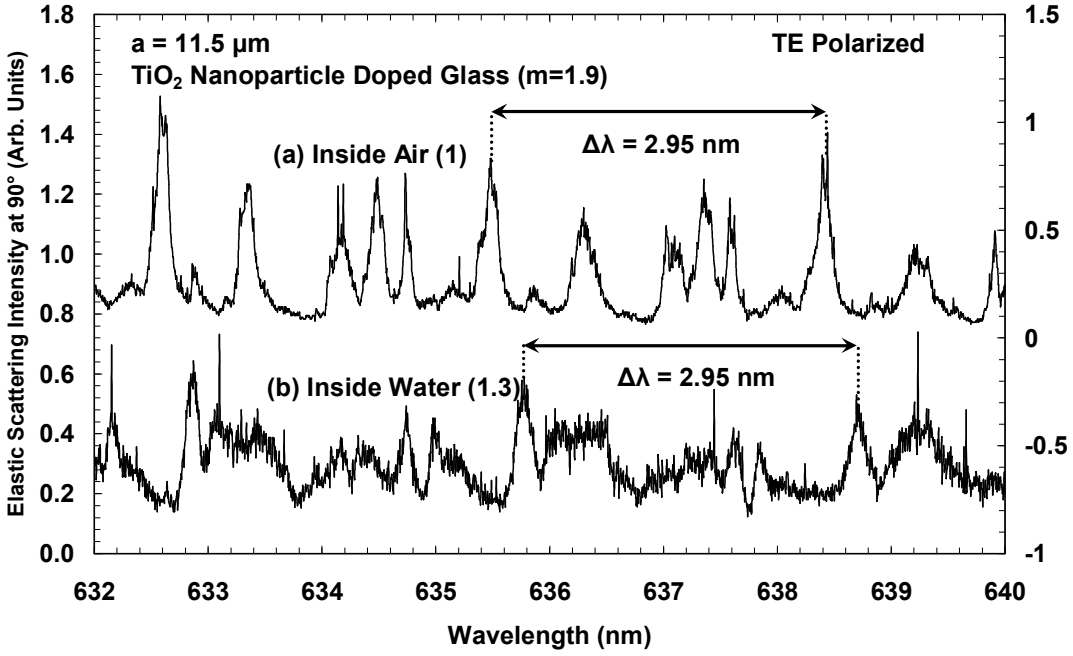

Figure 4.18 Elastic light scattering spectra of the microsphere in (a) air and (b) water.

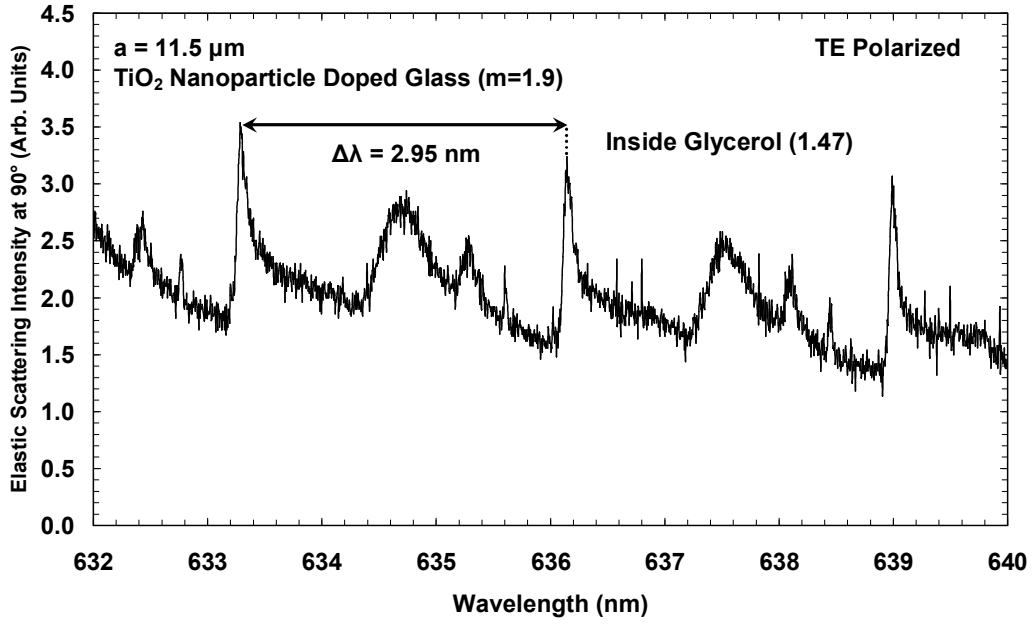

Figure 4.19 Elastic light scattering spectrum of the microsphere in glycerol.

sonances. After water evaporation, contaminant losses increase (Q_{cont}^{-1}). When, the whole surface is coated by water molecules, there will be no inhomogeneities because of contaminants, but radiation loss will increase for the high refractive index of water. These two effects are competing factors, that are responsible for the change of Q-factor. The relative stability of Q-factor may be because of equal contribution of these two factors. However, in the third measurement, (shown in Fig. 4.19) the Q-factor is increased for one radial mode. Addition of glycerol on the microsphere solves the contaminant problem.

In Fig. 4.20, the same experiment is performed with another microsphere. Since the microspheres are non identical, this time mode spacing is 3.244 nm. The Q-factor of resonances for the elastic spectrum of the microsphere in water is much higher than the spectrum in air in this case. This might be caused by the contaminant losses after the evaporation of water. Contaminant losses seem to dominate to the other losses.

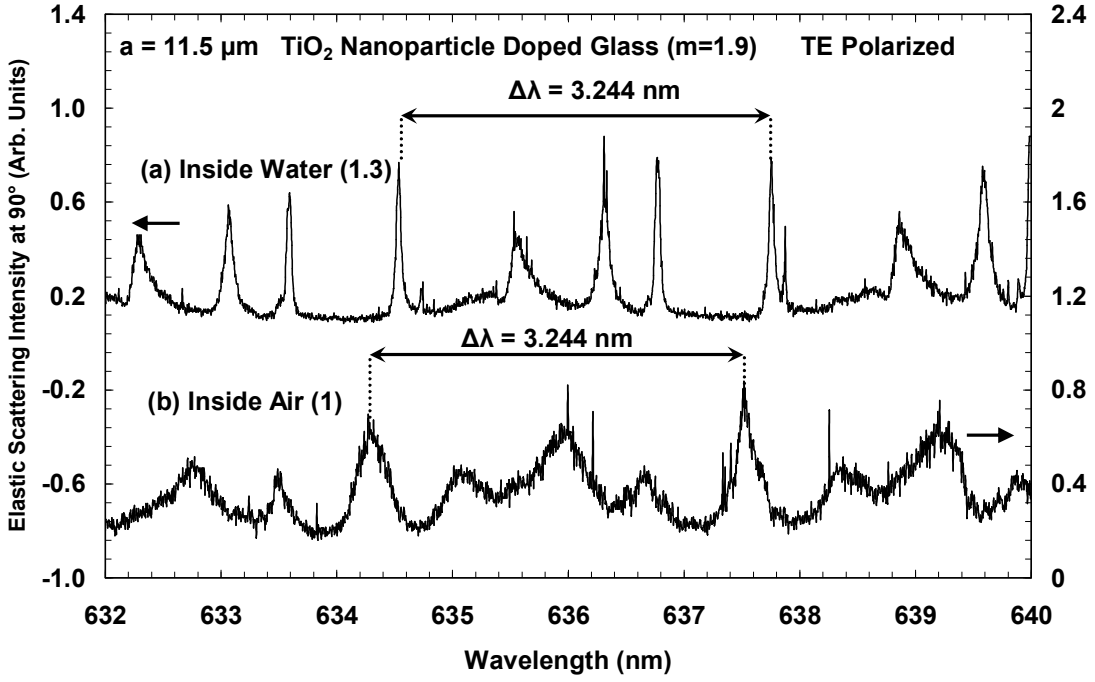

Figure 4.20 Elastic light scattering spectra of the microsphere in (a) water and (b) air.

In Fig. 4.21, there is a rise in background signal after placing glycerol on the OFHC. In addition, the resonance signal is enhanced by non-resonant coupling. However, there is no significant change in the Q-factor of the resonances. The mode spacing is measured to be 2.55 nm, which means a slightly bigger microsphere than the previous ones.

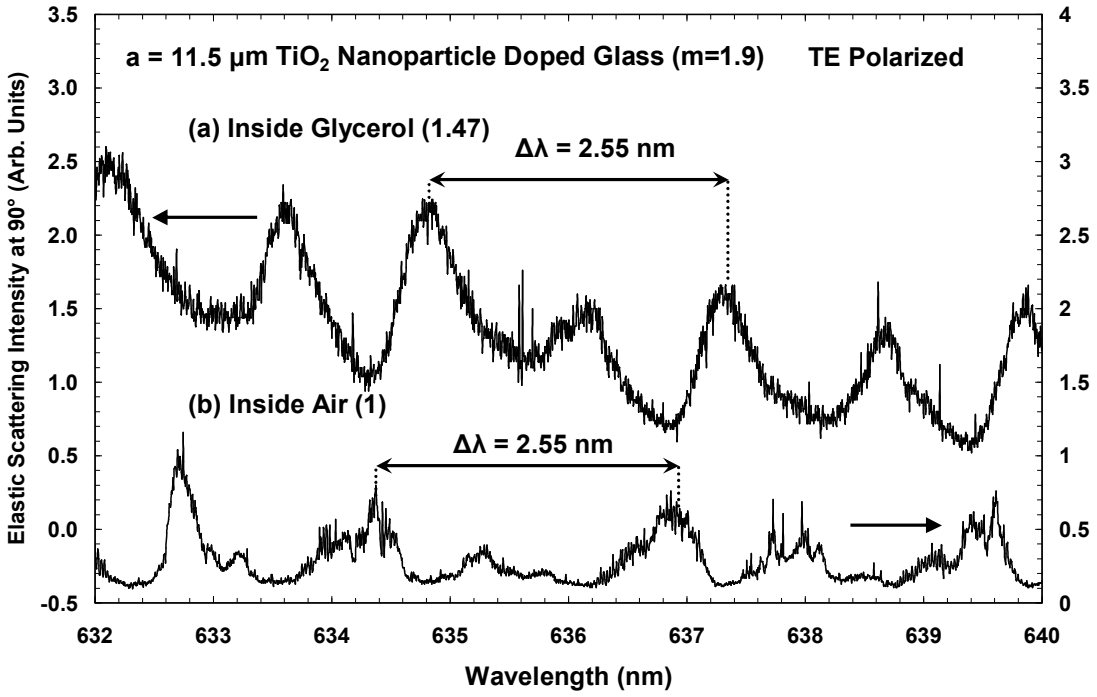

Figure 4.21 Elastic light scattering spectra of the microsphere in (a) glycerol and (b) air.

4.7 Elastic Light Scattering from Microspheres in Liquid Crystal

In this part, elastic light scattering spectra of microspheres with diameters of 23 μm and 103 μm in air and in LC is performed.

The sample of first experiment consists of a single mode optical fiber half coupler (OFHC), a high refractive index glass microsphere with a diameter of 23 μm, and 4-cyano-

4'-pentyl-biphenyl (5CB) LC. The laser light is coupled through the OFHC to the microsphere. Elastic light scattering at 90° is detected using a photomultiplier tube (PMT).

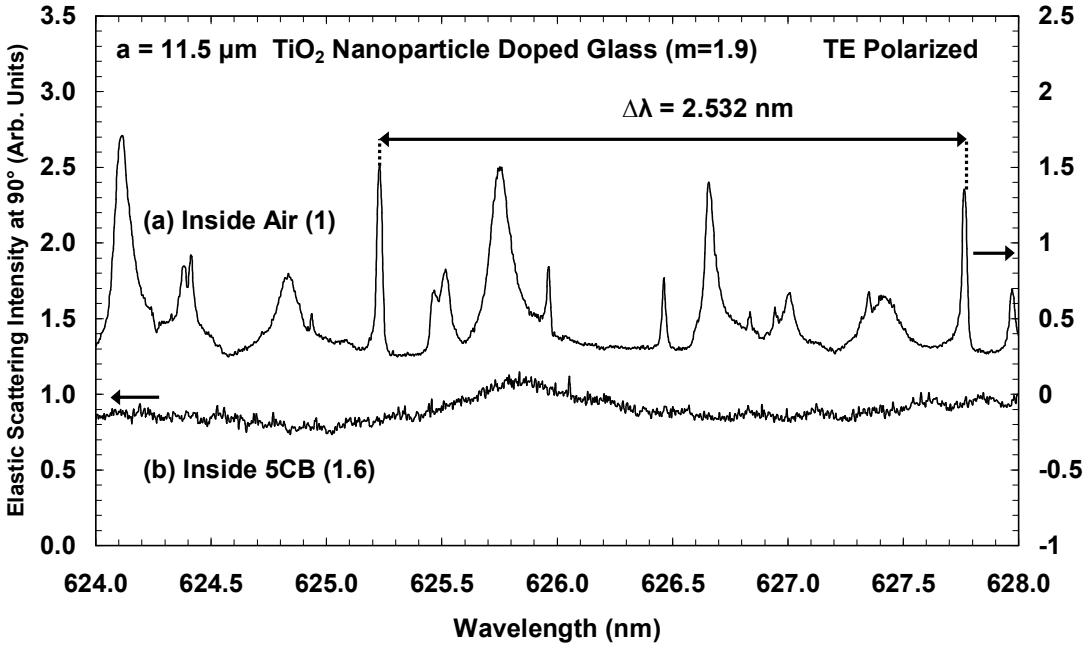

Figure 4.22 Elastic light scattering spectra of the microsphere in (a) air and (b) 5CB LC.

First, the spectrum of the microsphere is measured in the range of 624 nm and 628 nm. The mode spacing is measured as 2.532 nm. Then, a droplet of 5CB is placed on the fiber to surround the microsphere. After measuring the spectrum in the same range, a dramatic change in the spectrum is observed. The background signal increased and the Q-factor of the resonances decreased excessively. The background signal means non-resonant coupling in the microsphere - fiber system. As mentioned previously, the core refractive index of the fiber is 1.47, which is much less than both refractive indices of 5CB (n_o = 1.53 and n_e = 1.71). The high refractive index of the fluid between the microsphere and the optical fiber causes light to escape, before coupling to MDR's of the microsphere. In addition to the

increase of the background signal, the decrease of the Q-factor is a result of increasing coupling loss (Q_e^{-1}). The geometry of the microsphere, fiber and LC is shown in Fig. 4.23.

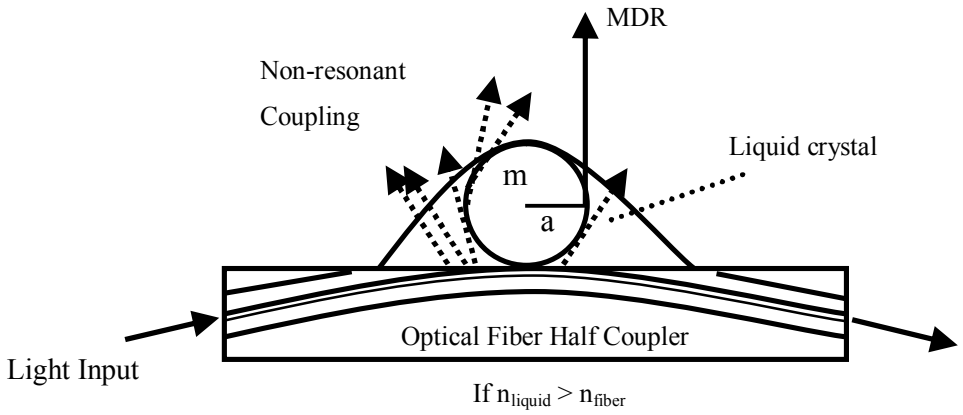

Figure 4.23 The schematic of non-resonant coupling.

In order to overcome the non-resonant coupling problem, another geometry is used. This time, the sample consists of a single mode optical fiber half coupler (OFHC), a high refractive index glass microsphere with a diameter of 103 μm, a glass slab, and 4-cyano-4'-pentyl-biphenyl (5CB) LC. The glass slab is holding the LC and the position of the slab is controlled by a micropositioner to place LC to the top of the microsphere. Microsphere with a larger diameter is used in order to prevent contact of LC with the optical fiber.

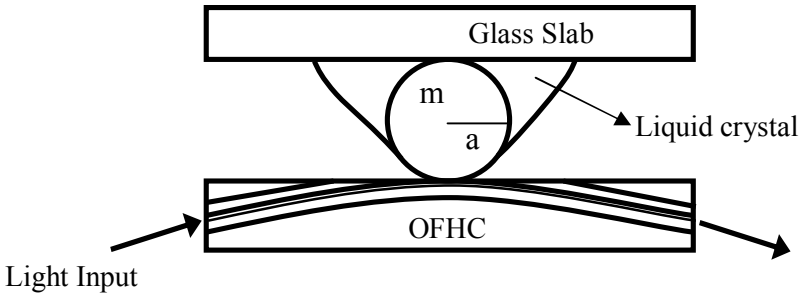

Figure 4.24 Illustration of the microsphere, optical fiber and LC geometry for efficient MDR coupling.

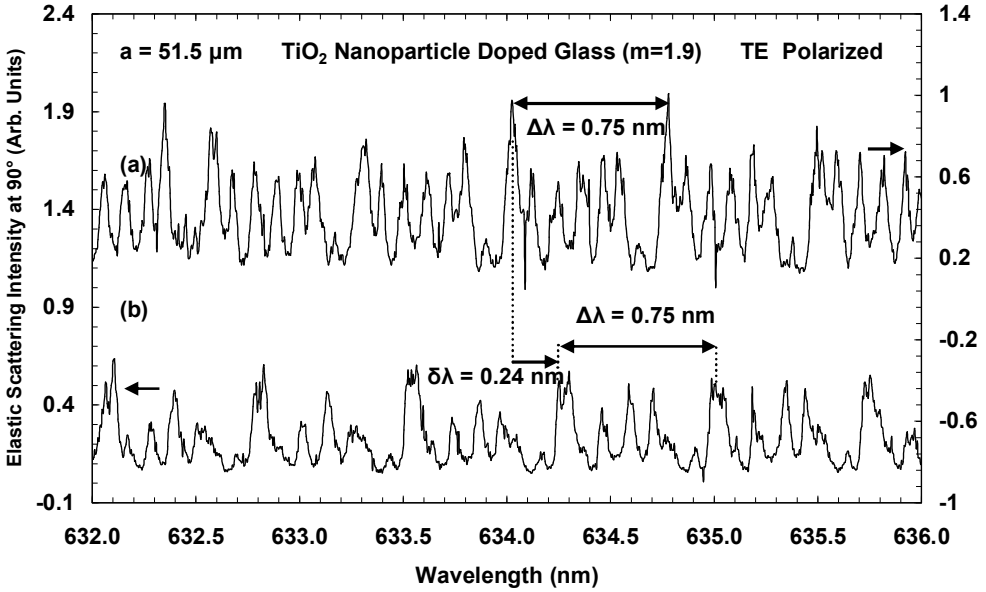

Figure 4.25 Elastic light scattering spectrum, when there is (a) no LC on the microsphere, and (b) 5CB LC on the microsphere. A red shift of 0.24 nm observed. The mode spacing is measured to be 0.75 nm in both cases.

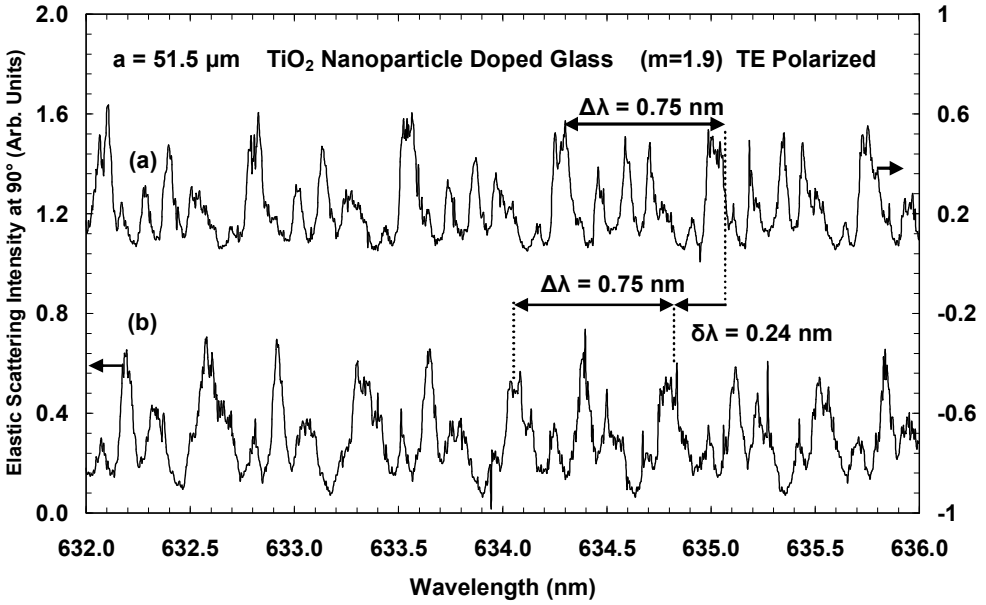

Figure 4.26 Elastic light scattering spectrum, when there is (a) 5CB LC on the microsphere, and (b) LC is removed from the microsphere. A blue shift of 0.24 nm is observed. The mode spacing is measured to be 0.75 nm in both cases.

First, the spectrum of the microsphere is measured at 90°. Then, LC is placed by glass slab over the microsphere and the spectrum at the same range is measured at 90°. Lastly, the LC is removed by taking the glass slab far from the microsphere. The contact area of LC to the slab is much larger than the contact area to the microsphere, so nearly all of the LC molecules are removed.

In Fig 4.25, it is clearly seen that, a red shift of optical resonances occurs due to 5CB LC on the surface of the microsphere. The red shift means an increase in the optical path. Despite the higher refractive index of the microsphere, when compared with the 5CB LC, an increase is observed on the optical path. This is caused by the weaker confinement of the evanescent field, when the LC coats the microsphere. The relative refractive index decrease and the geometrical path increase are competing effects and geometrical path increase should be higher for the microcavity.

In Fig. 4.26, removal of the 5CB LC, shifted the optical resonances to blue. However, the optical resonances do not appear same even the resonances are at the same wavelengths. This may be caused by a small amount of LC that could not be removed, or there might be contaminants. These LC form scattering centers on the surface and decreases the quality factor of the resonator, which can be described by losses due to surface contaminants (Q_{cont}^{-1}).

In conclusion, the red/blue shift of the optical microsphere resonance is realized by placing/removing a coat of 5CB LC on the surface of the microsphere. Instead of placing/removing LC of the surface, one can imagine electrically switching the LC and changing its refractive index, and thereby modulating the elastically scattered signal.

Chapter 5

CONCLUSIONS AND FUTURE WORK

In this work, applications of microcavities and advantages of microsphere cavities are indicated. An introduction to light scattering by spherical particles in geometric and wave optics is performed. Morphology dependent resonances are defined using "special" Lorenz-Mie theory. Afterwards, a brief explanation of generalized Lorenz-Mie theory is introduced. Properties of morphology dependent resonances and techniques to couple the resonances to the microspheres are presented by the necessary equations and explanations.

In the next chapter, a special phase of matter that exists between solids and liquids, nematic liquid crystal is mentioned. The anisotropy in structural, optical and electrooptical properties of liquid crystal molecules are explained.

Before the presentation and discussion of the experiments, the light sources and the steps to make them operational are discussed. Next, the relation of the impact parameter to the microsphere – optical fiber position is studied. A decrease is observed as the separation between the microsphere and the optical fiber increases. No change is experienced in Q-factor of the MDR's. Then, morphology dependent resonances of microspheres with diameters of 23 μm and 55 μm are measured for both TE and TM polarized light. Intra and interpolarization mode spacing, which show a good agreement with the calculations are determined. It is showed that, interpolarization mode spacing is much more sensitive than intrapolarization mode spacing to the medium refractive index. Moreover, the Q-factor of MDR's are measured to be on the order of 10^4.

Continuing experiments included the behaviour of MDR's in different fluid media. Q-factor of resonances inside water were observed to be higher than inside air. This might be caused by the domination of contaminant losses in air over other losses in water. Contaminant loss becomes dominant, when the water is evaporated, because of the leftover contaminants on the surface of the microsphere. Moreover, the Q-factor of the microsphere

increased by placing glycerol, after the evaporation of water. Glycerol decreases the contaminant losses. In addition, when the refractive index of fluid is higher than the refractive index of optical fiber, non-resonant coupling is observed. The non-resonant coupling increases background signal and decreases Q-factor of the microspheres. Placing the liquid crystal on the top of the microsphere overcame the non-resonant coupling. A 0.24 nm red/blue shift of MDR's is observed by placing/removing the nematic LC on the microsphere. High refractive index OFHC can also solve this problem.

In future, MDR's can be tuned by controlling the orientation of nematic liquid crystals by an external electric field. This will open a gateway to new generation of liquid crystal switches, modulators, or active filters based on microspheres. Another interesting application of the microsphere inside liquid crystal system might be the measurement of phase transitions in liquid crystals using MDR's.

APPENDIX A

A.1 Control and Data Acquisition Software

In this appendix, instructions of software by National Instruments LabView® developed for grating position control of the Lambda Physik dye laser and data acquisition from Tektronix digital data storage oscilloscope (DSO) are introduced.

The dye laser interface is connected to the computer by a general purpose interface board (GPIB). The software also includes an etalon scan option, which should be updated. There are three stepper motors on the dye laser. The first one, which can be controlled by the software, controls the grating position, the second one controls the etalon position, and the third one controls the second harmonic generation (SHG) crystal position. In this section, the control of the grating stepper motor is explained. There are two main functions in the software; grating position control and grating scan.

When the interface of the dye laser is restarted, the grating stepper motor goes to the step number 285715 automatically. By the grating position function, the stepper motor can be positioned in any step number.

Grating scan is the function used for spectroscopy with the dye laser. The data can be taken thorough either universal serial bus (USB) or GPIB to the computer. The software takes the maximum data point captured in the DSO or the mean value of the captured data. This can be selected in the panel showed in Fig. A.1.1 by “peak to peak” or “mean”. In the experiments, the measurements are done by a photomultiplier tube (PMT) or a silicon photodiode (PD) connected to a DSO with GPIB bus. In Fig. A1.2 the oscilloscope bus selection is shown. Scan parameters such as start position, end position, step size, and wait time can be entered in the software. In Fig. A.1.3, the scan parameters are shown. In every step of the motor, the number of data to take can be entered to the panel shown in Fig.

A.1.4. The software takes the mean of data number automatically. During the scan, a real time plot is drawn as step number versus voltage. The plot screen is shown in Fig. A.1.5.

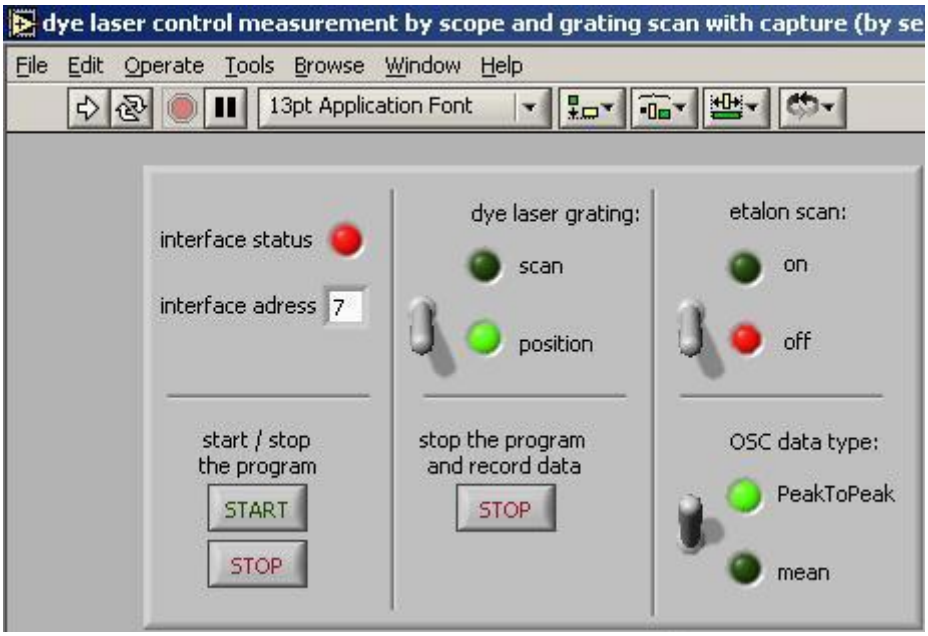

Figure A.1.1 Interface status panel.

Run Button: Starts the software.

Note: *Do not start the software before turning on the dye laser control interface.*

Interface Status: Shows the connection to interface.

Interface Address: Shows the address of the interface.

Dye laser grating: Choose either scan or position control of the grating.

Etalon Scan: Choose off (Not updated).

Start / stop the program: Start / stop scan or position control.

Stop the program and record data: Stops the scan and records the data taken from DSO**.**

OSC Data Type: Read the maximum point or the mean of the points captured in the DSO.

Figure A.1.2 Oscilloscope selection panel.

VISA resource name: Select the appropriate VISA.

VISA resource name 2: Select the second appropriate VISA.

OSC capture:

On: Capture the OSC screen.

Off: Do not capture the OSC screen.

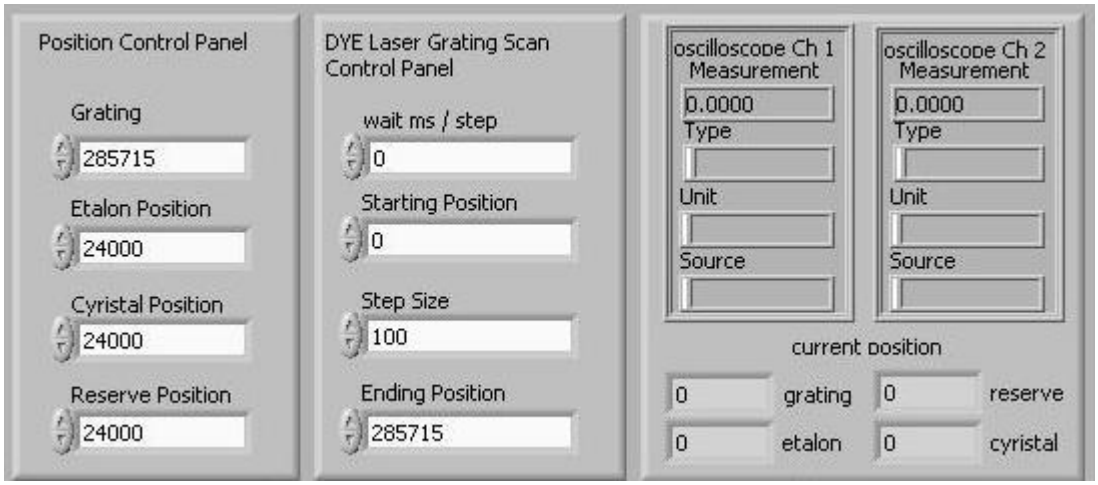

Figure A.1.3 Scan parameter and status panel.

Position Control Panel: You can directly send grating to any position between 0 and 285715.

Dye Laser Grating Scan Control Panel:

Wait ms / step: Enter a value to adjust the scan rate.

Starting Position: Start position of the stepper motor.

Step Size: Step size of the stepper motor.

Ending position: Ending scan position of the stepper motor.

Oscilloscope Channel 1 Measurement: Shows the status of OSC CH 1.

Oscilloscope Channel 2 Measurement: Shows the status of OSC CH 2.

Current Position: Shows the current position of stepper motors.

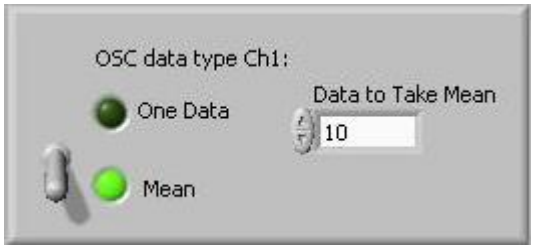

Figure A.1.4 Integration time adjustment panel.

OSC # data Type Ch#:

One data: Takes one data from OSC # Ch #

Mean: Takes the mean of data to take mean #.

Figure A.1.5 Real time data plot screen (data not shown).

Voltage Chart from OSC # ch #: Plots the data in OSC # ch # as voltage versus grating position in real time.

VITA

Hasan Yılmaz was born in Çanakkale, Turkey in 1985. He completed the high school in Çanakkale Milli Piyango Anadolu Lisesi, Çanakkale, Turkey in 2003.

He received his B. Sc. degree in Physics Engineering from Istanbul Technical University (ITU), Istanbul, Turkey, in 2008. He worked on 'Temperature Dependence of Atomic Step Free Energy on Si(001) Surface'' at ITU as his undergraduate thesis with Asst. Prof. Oğuzhan Gürlü.

Later he joined the M.Sc. program in Materials Science and Engineering at Koç University in Istanbul, Turkey in 2008, as a teaching/research assistant during which, he worked on "Optical Resonances of Glass Microspheres in Amorphous and Crystalline Liquids" with Prof. Ali Serpengüzel.

As of spring 2011, he plans to continue his Ph.D. work at the Institute for Nanotechnology (MESA+), University of Twente, Enschede, The Netherlands. He is expected to work with Dr. Allard P. Mosk on ''The propagation of light in disordered or ordered photonic nanostructures in the presence of optical loss and gain''.

BIBLIOGRAPHY

[1] Lord Rayleigh, "The Problem of the Whispering Gallery," Scientific Papers (Cambridge University), **5**, 617 (1912).

[2] C. J. Hood, T. W. Lynn, A. C. Doherty, A. S. Parkins, and H. J. Kimble, "The Atom-Cavity Microscope: Single Atoms Bound in Orbit by Single Photons," Science **287**, 1447 (2000).

[3] A. M. Mintairov, Y. Chu, Y. He,S. Blokhin, A. Nadtochy, M. Maximov, V. Tokranov, S. Oktyabrsky, and J. L. Merz, "High-Spatial-Resolution Near-Field Photoluminescence and Imaging of Whispering-Gallery Modes in Semiconductor Microdisks with Embedded Quantum Dots," Phys. Rev. B. **77**, 195322 (2008).

[4] P. Dong, S. F. Preble, J. T. Robinson, S. Manipatruni, and M, Lipson, "Inducing Photonic Transitions between Discrete Modes in a Silicon Optical Microcavity," Phys. Rev. Lett. **100**, 033904 (2008).

[5] A. Badolato, K. Hennessy, M. Atatüre, J. Dreiser, E. Hu, P. M. Petroff, and A. Imamoğlu, "Deterministic Coupling of Single Quantum Dots to Single Nanocavity Modes," Science **308**, 1158 (2005).

[6] M. Hossein-Zadeh and K. J. Vahala, "Free Ultra-High-Q Microtoroid: A Tool for Designing Photonic Devices," Opt. Express **15**, 166 (2007).

[7] A. Serpengüzel, S. Arnold, and G. Griffel, "Excitation of Resonances of Microspheres on an Optical Fiber," Opt. Lett. **20**, 654 (1995).

[8] T. Ioppolo, M. Kozhevnikov, V. Stepaniuk, M. V. Ötügen, and V. Sheverev, "Micro-Optical Force Sensor Concept Based on Whispering Gallery Mode Resonators," Appl. Opt. **47**, 3009 (2008).

[9] T. Ioppolo, U. Ayaz, and M. V. Ötügen, **"**Tuning of Whispering Gallery Modes of Spherical Resonators Using an External Electric Field," Opt. Express **17**, 16465 (2009).

[10] C.-H. Dong, L. He, Y.-F. Xiao, V. R. Gaddam, S. K. Ozdemir, Z.-F. Han, G.-C. Guo, and L. Yang , "Fabrication of High-*Q* Polydimethylsiloxane Optical Microspheres for Thermal Sensing," Appl. Phys. Lett. **94**, 231119 (2009).

[11] E. Yüce, O. Gürlü, and A. Serpengüzel, "Optical Modulation with Silicon Microspheres," IEEE Photon. Technol. Lett. **21**, 1481 (2009).

[12] A. A. Savchenkov, W. Liang, A. B. Matsko, V. S. Ilchenko, D. Seidel, and L. Maleki, "Tunable Optical Single-Sideband Modulator with Complete Sideband Suppression," Opt. Lett. **34**, 1300 (2009).

[13] S. Arnold, M. Khoshsima, I. Teraoka, S. Holler, and F. Vollmer, "Shift of Whispering Gallery Modes in Microspheres by Protein Adsorption," Opt. Lett. **28**, 272 (2003).

[14] I. M. White, N. M. Hanumegowda, H. Oveys, and X. Fan, "Tuning Whispering Gallery Modes in Optical Microspheres with Chemical Etching," Opt. Express **13**, 10754 (2005).

[15] P. Zijlstra, K. L. van der Molen, and A. P. Mosk, "Spatial Refractive Index Sensor Using Whispering Gallery Modes," App. Phys. Lett. **90**, 1611001 (2007).

[16] N. M. Hanumegowda, C. J. Stica, B. C. Patel, I. White, and X. Fan, "Refractometric Sensors Based on Microsphere Resonators," Appl. Phys. Lett. **87**, 201107 (2005).

[17] G. Gilardi, D. Donisi, A. Serpengüzel, and R. Beccherelli, "Liquid-Crystal Tunable Filter Based on Sapphire Microspheres," Opt. Lett. **34**, 3253 (2009).

[18] M. Humar, M. Ravnik, S. Pajk, and I. Musevic, "Electrically Tunable Liquid Crystal Optical Microresonators," Nature Photonics **3**, 595 (2009).

[19] H. Yokoyama, "Liquid Crystals: Tunable Whispers," Nature Photonics **3**, 560-561 (2009).

[20] H. M. Nussenzveig, "Diffraction Effects in Semiclassical Scattering," Cambridge University Press, Cambridge (1992).

[21] E. Hecht, "Optics," Addison Wesley Longman Inc., London (2002).

[22] H.C. van de Hulst, "Light Scattering by Small Particles," Dover, New York (1981).

[23] C. F. Bohren and D. R. Huffman, "Absorption and Scattering of Light by Small Particles," Interscience, New York (1983).

[24] P. Barber and S. C. Hill, "Light Scattering by Particles: Computational Methods," World Scientific, Singapore (1990).

[25] G. Roll and G. Schweiger, "Geometrical Optic Model of Mie Resonances," J. Opt. Soc. Am. A. **17**, 1301 (2000).

[26] J. A. Lock and G. Gouesbet, "Generalized Lorenz–Mie Theory and Applications," J. Quant. Spectrosc. Radiat. Transfer **110**, 800 (2009).

[27] A. Serpengüzel and A. Demir, "Silicon Microspheres for Near-IR Communication Applications," Semicond. Sci. Technol. **23**, 064009 (2008).

[28] S. Schiller and R. L. Byer, "High-Resolution Spectroscopy of Whispering Gallery Modes in Large Dielectric Spheres," Opt. Lett. **16**, 1138 (1991).

[29] B. E. Little, J. P. Laine, and H. A. Haus, "Analytic Theory of Coupling from Tapered Fibers and Half-Blocks into Microsphere Resonators," J. Lightwave Technol. **17**, 704 (1999).

[30] M. L. Gorodetsky, A. A. Savchenkov, and V. S. Ilchenko, "Ultimate Q of Optical Microsphere Resonators," Opt. Lett. **21**, 453 (1996).

[31] M. L. Gorodetsky and V. S. Ilchenko, "Optical Microsphere Resonators: Optimal Coupling to High-*Q* Whispering-Gallery Modes," J. Opt. Soc. Am. B. **16**, 147 (1999).

[32] A. Chiasera, Y. Dumeige, P. Feron, M. Ferrari, Y. Jestin , G. N. Conti, S. Pelli, S. Soria, and G. C. Righini, "Spherical Whispering-Gallery-Mode Microresonators," Laser Photon. Rev. **4**, 457 (2009).

[33] B. E. Little, J.-P. Laine, D. R. Lim, H. A. Haus, L. C. Kimerling, and S. T. Chu, "Pedestal Antiresonant Reflecting Waveguides for Robust Coupling to Microsphere Resonators and for Microphotonic Circuits," Opt. Lett. **25**, 73 (2000).

[34] J. E. M. Goldsmith and J. E. Jawler , "Optogalvanic Spectroscopy," Contemp. Phys. **22**, 235 (1981).

[35] D. S. King, P. K. Schenk, K. S. Smith, and J. C. Travis, "Direct Calibration of Laser Wavelength and Bandwidth Using the Optogalvanic Effect in Hollow Cathode Lamp," Appl. Opt. **16**, 2617 (1977).

[36] R. A. Keller, R. Engleman, and B. A. Palmer, "Atlas for Optogalvanic Wavelength Calibration," Appl. Opt. **19**, 836 (1980).

[37] S. Levesque, F. Babin, and J.-M. Gagne, "Calibration of Pulsed Laser Wavelength by Optogalvanic Spectroscopy in Hollow Cathode Discharges," IEEE Trans. Instrum. Meas. **42**, 251 (1993).

[38] V.K. Saini, V.K. Shrivastava, R. Khare, "Anomalous Behavior of Optogalvanic Signal in a Miniature Neon Discharge Lamp," Opt. Comm. **281**, 129 (2008).

[39] Exciton Laser Dyes, Dayton, Ohio 45437.

[40] Y. Panitchob,G. S. Murugan, M. N. Zervas, P. Horak, S. Berneschi, S. Pelli, G. N. Conti, and J. S. Wilkinson, "Whispering Gallery Mode Spectra of Channel Waveguide Coupled Microspheres," Opt. Express **16**, 11066 (2008).

[41] P. G. de Gennes and J. Prost, "The Physics of Liquid Crystals," Clarendon Press, Oxford (1993).

[42] P. J. Collings and M. Hird, "Introduction to Liquid Crystals," Taylor and Francis Ltd. London (1998).

[43] H. Kelker and B. Scheurle, "A Liquid-Crystalline (Nematic) Phase with a Particularly Low Solidification Point," Angew. Chem. Int. Ed. **8**, 884 (1969).

[44] G. W. Gray, K. J. Harrison, J A. Nash, "New Family of Nematic Liquid Crystals for Displays," Electron. Lett. **9**, 130 (1973).

[45] J. Martz, L. Zuppiroli, and F. Nüesch, "Benzoic and Aliphatic Carboxylic Acid Monomolecular Layers on Oxidized GaAs Surface as a Tool for Two-Dimensional Photonic Crystal Infiltration," Langmuir **20**, 11428 (2004).

[46] E. Lueder, "Liquid Crystal Displays: Addressing Schemes and Electro-Optical Effects," Wiley, West Sussex (2001).

[47] C. Wen, S. Gauza, R. Lu, and S. Wu, "Refractive Indices of Liquid Crystals for Display Applications," IEEE/OSA J. Display Technol. **1**, 51 (2005).

[48] A. Bogi and S. Faetti, "Elastic, Dielectric and Optical Constants of 4'-pentyl-4-cyanobiphenyl," Liquid Crystals **28**, 729 (2001).

[49] L. M. Blinov and V. G. Chigrinov, “Electrooptic Effects in Liquid Crystal Materials,” Springer-Verlag, NewYork (1994).